Reconstruction of Mars2020 Backshell Radiative Heating via Infrared Emission Spectroscopy of $CO_2/N_2/Ar$ Shockwaves

Augustin C. Tibere-Inglesse[1]
NASA Postdoctoral Fellow at NASA Ames Research Center, Mountain View, CA, 94035, USA

Thomas K. West IV[2]
NASA Langley Research Center, Hampton, VA, 23681, USA

Christopher C. Jelloian[3], Nicolas Q. Minesi[4], R. Mitchell Spearrin[5]
University of California, Los Angeles (UCLA), Los Angeles, CA 90095, USA

Justin Clarke[6], Luca di Mare[7], Matthew McGilvray[8]
University of Oxford, England OX2 0ES, UK

Brett A. Cruden[9]
AMA Inc at NASA Ames Research Center, Mountain View, CA, 94035, USA

A test series was performed in the Electric Arc Shock Tube (EAST) facility, with the aim of reproducing flight conditions encountered during the Mars2020 mission entry into Mars atmosphere. For this test series, the EAST facility was instrumented with two spectrometers for Optical Emission Spectroscopy (OES) measurements and three mid-infrared lasers for Tunable Diode Laser Absorption Spectroscopy (TDLAS). This paper focuses on the spectrally and spatially resolved radiance measured with OES. Conditions were chosen to achieve similarity to backshell radiative heating measured with the MEDLI2 heat flux gauges near and after the time of peak heating. Comparisons were made against two candidate kinetic models for Mars entry. Below 2.7 km/s, the

---

[1] Postdoctoral Fellow, Aerothermodynamics Branch
[2] Aerospace Engineer, Vehicle Analysis Branch, Systems Analysis and Concepts Directorate. Member AIAA
[3] Ph.D. Student, Mechanical and Aerospace Engineering Department, Member AIAA.
[4] Postdoctoral Researcher, Mechanical and Aerospace Engineering Department, Member AIAA.
[5] Assistant Professor, Mechanical and Aerospace Engineering Department, Member AIAA.
[6] Ph.D. Student, Oxford Thermofluids Institute, Department of Engineering Science.
[7] Associate Professor, Oxford Thermofluids Institute, Department of Engineering Science.
[8] Associate Professor, Oxford Thermofluids Institute, Department of Engineering, Member AIAA
[9] Senior Research Scientist, Aerothermodynamics Branch, and Associate Fellow AIAA.

chemistry is effectively frozen, with measurements being above both models and CEA predictions. It is shown that taking into account shock deceleration in the tube explains most of the discrepancy between measured and frozen radiance. For velocities above 2.7 km/s, the data lies between the two models. However, adjusting for shock deceleration indicates that one of the models may be preferred for predicting CO_2 dissociation. Finally, comparison between OES and TDLAS data are made and show a good agreement on the measured temperature and CO_2 number density profiles, typically within 10 and 5%, respectively. A good agreement is also observed for the radiance that would be inferred based upon the quantities measured by TDLAS.

I. Introduction

On February 18, 2021, the NASA Mars 2020 mission successfully landed the Perseverance rover onto the surface of Mars. During entry into the Martian atmosphere, the Mars Entry, Descent, and Landing Instrumentation 2 (MEDLI2) sensor suite collected in-flight pressure, temperature, and heat flux data on the aeroshell [1] [2]. Of particular relevance to this work, MEDLI2 included two total heat flux sensors and one radiometer to directly measure the convective and radiative heating on the afterbody. A comparison between the measured [3] and predicted radiative heat flux – using two different kinetic models, referred to as “Cruden” [4] and “Johnston” [5] (the latter one having a faster CO_2 dissociation rate) – at the leeside sensor MTB08 location is presented in Figure 1. Solid lines depict the radiative heating predictions, with the dashed line showing the impact of convective heating for one of the models. [3] In general, the Cruden mechanism gives a good agreement with the data throughout most of the heat pulse. At later times in the pulse, the Johnston mechanism gives a slightly better agreement. Comparison between predicted and measured radiative fluxes were also made using the co-located MTB09 radiometer and showed disagreement increasing up to 50% with time from entry interface, which can be attributed to blockage by ablation products [3]. Previous measurements during the Schiaparelli capsule entry also showed good agreement (within 16%) between measured and computed back shell heating but the complete dataset was not recovered due to the failed landing of Schiaparelli [6].

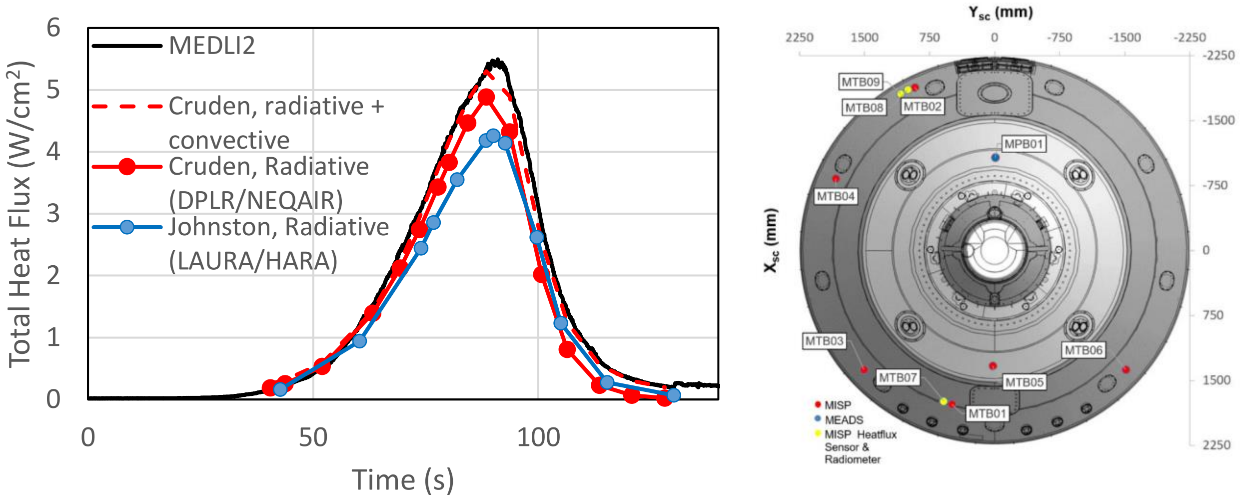

Figure 1: Left: Comparison between the flight heat flux measurement with the MTB08 sensor, and the radiative heat flux prediction using the Cruden [4] or Johnston [5] kinetic model. The impact of convection for the Cruden model is shown in the dashed line. Adapted from Ref. [3]. Right: Location of the sensor in the Mars2020 backshell [2].

Reproduction of flight conditions in ground test facilities is of interest for isolating heating mechanisms and may provide additional data that allows for validation of predictive models. A test series was previously conducted in the Electric Arc Shock Tube (EAST) facility at NASA Ames Research Center for the Mars Science Laboratory and was able to reconcile most of the discrepancy in stagnation line heating measured by the original MEDLI sensors [7]. However, no similar test has been performed that is relevant to heating on the afterbody. Such a test of the Mars2020 mission is motivated by the difference in the predictions observed in Figure 1 and a desire to independently confirm the heating data. It has recently been shown that the radiation on the afterbody of a capsule could be modeled by radiation of an oblique shock [8]. This method, known as shock tube informed bias, states that the oblique shock has similarity with an incident shock when the normal component of velocity and particle time behind the shock are matched. This similarity is used here to find shock tube conditions that are relevant to the Mars2020 backshell. Fifty-nine (59) shots were performed during this test series with velocities varying from 1.17 to 3.75 km/s and fill pressures (mostly) between 1.1 and 2.0 Torr. A summary of most of the shots performed is given in Figure 2. The pressures of 1.1, 1.5 and 2 Torr roughly correspond to flight times of 92, 101 and 144 s, respectively. These conditions were chosen to represent peak heating, half of the peak and closeout of the radiation pulse, as seen on Figure 1. Measurements of lower pressure conditions, corresponding to the rising portion of the heat pulse, will be conducted in a future test series using the 53 cm Low Density Shock Tube which was recently installed in the EAST facility. This paper will present the results and analysis of the Optical Emission Spectroscopy (OES) measurements made during this test series. A companion paper [9] describes tunable diode laser absorption spectroscopy (TDLAS) performed during the same test.

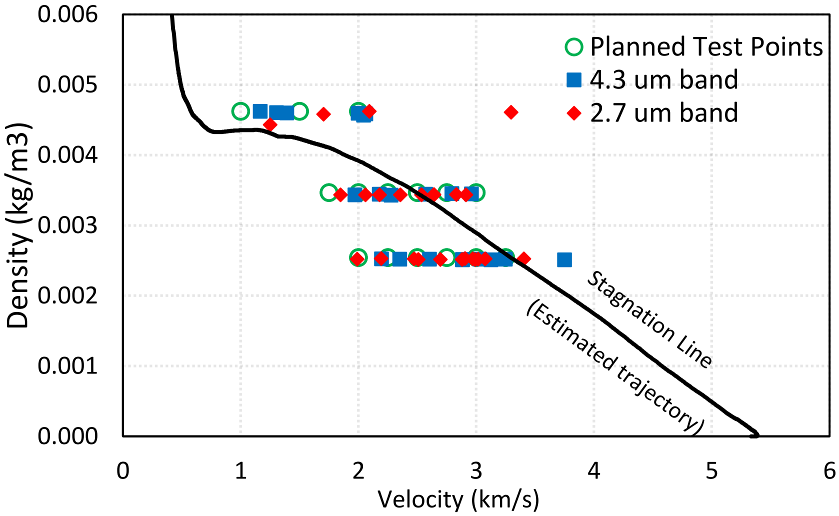

Figure 2: Summary of shots performed, with the two different infrared spectrometer settings (see section II). The conditions are chosen according to the shock tube informed bias methodology (circle) and the stagnation line trajectory (line) are also shown for comparison.

II. Experimental setup

The Electric Arc Shock Tube (EAST) facility has been described in detail in previous publications [10] [11]. This facility is composed of a 1.2 MJ, 40 kV capacitor bank that drives a 10.16 cm aluminum shock tube. The test gas consists of simulated Mars atmosphere – 95.4% CO_2, 2.6% N_2, 2.0% Ar. This composition is based upon measurements made on the Martian surface reported by Trainer et al. [12] throughout the Martian solar cycle at the same time of year as the Mars2020 entry, which differ from the often cited, but incorrect, initial measurements made with the same instruments [13]. A schematic of the EAST facility is presented in Figure 3. The test section of the facility is usually instrumented with four spectrometers looking at different wavelength regions: one in the Vacuum Ultraviolet, one in the UV/visible, one in the visible/near-infrared and one in the mid infrared [10], see Figure 4. However, based on the previous test series at similar conditions [7], no significant radiation is expected to be measured except in the mid infrared region. The measurements in this test therefore included data from only two cameras, looking at UV/visible and infrared emission, respectively. The radiation in the UV/visible consisted of weak continuum radiation and is not analyzed in this paper. Only the data from the IR camera will be presented. Two different settings for the infrared spectrometer were studied to measure the 4.2 μm fundamental and 2.7 μm overtone bands of CO_2 which are the main source of radiation in Mars entry. Tunable Diode Laser Absorption Spectroscopy (TDLAS) was also implemented for this test series and results are presented in a companion paper [9]. A summary of all shots performed with useable emission data is given in Appendix A.

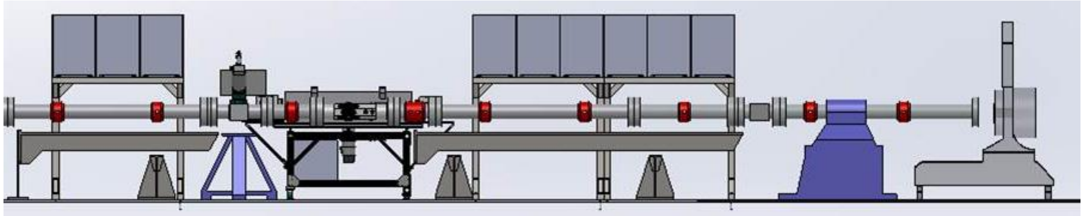

Figure 3: Schematic of the EAST facility.

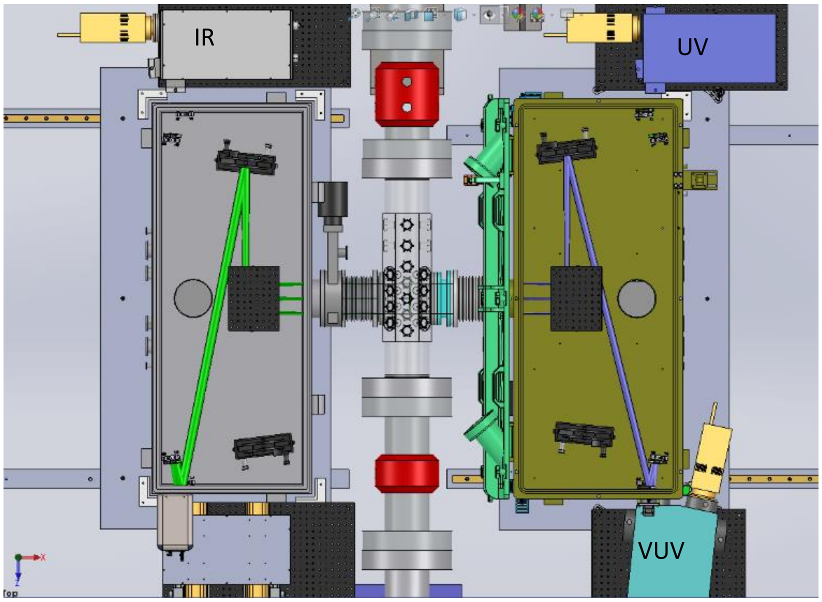

Figure 4. Instrumentation setup of the test section for OES.

III. Approach

An example of experimental data obtained from this campaign, denoted as Test 64, is presented in Figure 5. The data are spectrally and spatially resolved, giving a 3D map of radiance versus these two variables. Horizontal and vertical slices shown in Figure 5 represent the integrated radiance versus wavelength and position, respectively. Two measurements are shown, corresponding to the two CO_2 bands measured in this campaign. The vertical slices are used to get an estimate of the shock front location. The position is shown in lab frame coordinates. The shock front location depends upon trigger level and timing and thus may differ from shot to shot.

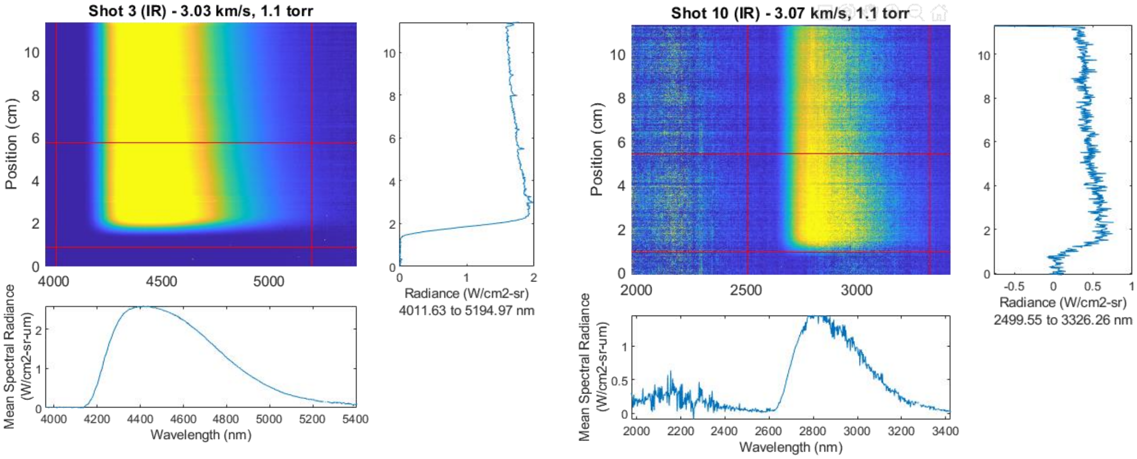

Figure 5: 3D spectral intensity maps obtained for shot 3 and 10 with the IR camera. Horizontal and vertical slices represent the integrated radiance versus wavelength and position, respectively, over the range highlighted by the red lines.

In this work, both the spectral radiance and the total radiance are compared with computational predictions. Comparisons of spectrally resolved data consist of the radiance binned over 1 cm, starting 2 cm after the shock front. This spectrum is then compared with NEQAIR [12] predictions, based on (chemical and thermal) equilibrium and frozen conditions computed using CEA [13] [14]. Comparison of the spatial variation is based on the radiance integrated over 4100-5400 nm or 2600-2800 nm, depending on the spectrometer setting and band being measured. The 4100-5400 nm range allows comparison to radiation from the fundamental 4.2 μm band of CO_2. At lower velocities, below 2 km/s, the wavelength range is reduced to 4100-4800 nm to prevent integrating noise signal. The 2600-2800 nm range is used for comparison of the 2.7 μm band. Even though this band was measured out to 3400 nm, the higher wavelength range was not used due to a poor signal to noise ratio above 2800 nm. Measurements below 2400 nm suffer from ambient absorption and are too noisy to discern signal, although some radiation is predicted to occur in this region. The measured radiance profiles are also binned over ±2 cm around the shock front – which was previously defined as the nonequilibrium radiance metric [14, 15], but will be referred to as the peak radiance in this paper – and compared with predictions.

CFD simulations were performed using DPLR [16] by extracting the stagnation line from a flow around a 1-m sphere simulation at freestream conditions equal to the test gas temperature and pressure and the measured velocity, in a similar way as in Refs [4, 17]. Two different kinetic models were used and are denoted as Johnston [5] and Cruden [4]. These models were previously tested mainly for velocities above 3 km/s, and this work may extend their validation range to lower velocity. For these velocities, the most relevant difference between the two models is the rate of CO_2 dissociation. Johnston uses the rate of Park [18], while Cruden uses that of Ebrahim [19]. In recent works [20], Clarke et al demonstrated that the time of flight for a simulation of a blunt body stagnation line can be different than the shock tube flow, due to the growth of the boundary layer in the post shock region, resulting in a slower core flow. The authors gave a spatial transformation to apply to the blunt body simulation to compare with shock tube data [20]. This transformation was used in all DPLR results.

It has previously been proposed that radiation in EAST, and other shock tube facilities, is affected by the deceleration of the shock wave as it traverses the tube [21]. This was experimentally verified by varying the shock history between accelerating and decelerating profiles for the same final shock speed in the Oxford T6 facility [22, 23]. The Oxford measurements showed that the test slug had significant enthalpy variation caused by the variation in shock profiles and boundary layer. From this work, the LASTA code [24] was developed to predict the influence of the shock deceleration on measurements made downstream in the shock tube. The methodology underpinning LASTA is the assumption that the shock trajectory approximates the complex wave processes present in a shock tube during a test. Therefore, for a given shock speed profile with a specified fill condition, the solver can reproduce the pressure and temperature variations present as a consequence of changes in shock speed. The gas can be assumed to be ideal or have equilibrium or frozen chemistry. The LASTA solver uses a quasi-one-dimensional, Lagrangian formulation in which uniformly distributed discrete gas slices are placed along the tube. As the shock propagates down the tube, the slices are activated and processed by the shock at the appropriate shock speed according to the specified trajectory. After this, forward and backward travelling waves (in the shock frame of reference) evolve the condition of the activated slices. The rearward-travelling waves are caused by changing post-shock conditions; the forward-travelling waves are comprised of driver pressure fluctuations, waves due to mass loss to the boundary layer, and waves caused by mixing and reflections at the contact surface. By tracking the waves as they traverse the test slug, their influence on each gas slice can be determined. It additionally predicts the test slug length. The LASTA approach accurately reproduces the experimental test slug, while taking a fraction of the time of a full axisymmetric simulation of the experiment. The LASTA code has recently been used to explain discrepancies discussed in previous EAST data [25]. The code is employed in this work to examine the effects of shock deceleration and wave propagation on the measured radiance. LASTA simulations were performed using the measured shock position versus time history obtained from the EAST time of arrival sensors. The LASTA outputs were then used as input to NEQAIR to obtain a radiance profile. In addition to CEA and CFD simulations, the measurements were compared with LASTA/NEQAIR results assuming frozen or equilibrium conditions. Additionally, for reacting cases, the LASTA simulations were used to obtain the shock velocity and enthalpy from which the gas at a given position behind the shock front originates. For each of these solutions, a 0D kinetic simulation is then performed with the Cantera code [26] over the time of flight returned by LASTA using either the Johnston [5] or Cruden [4] kinetic rate model. The time of flight is a combination of boundary layer effects changing the axial velocity and, to a lesser extent, shock speed variation down the tube [27, 28, 24]. Performing this calculation at different locations behind the shock then obtains a gas temperature and number density versus distance behind the shock. NEQAIR simulations are then performed with these results as inputs to get radiance profiles.

IV. Results

A. Typical comparisons between experiments and simulations

Typical comparison of integrated radiance profiles and spectra between measurements and simulations are presented in Figure 6-9 for high to low velocities at fill pressures of 1.1 and 1.5 Torr. The simulations include CEA/NEQAIR calculations assuming equilibrium and frozen conditions, DPLR/NEQAIR results using the Johnston or Cruden model and their corresponding LASTA/Cantera calculations.

For velocities higher than 2.7 km/s, the integrated radiance profile increases at the shock front then decreases towards its equilibrium value, as is expected in a reacting flow. At 1.1 Torr, the radiance peaks below the frozen value, while the frozen limit is obtained at 1.5 Torr. The measured radiance profile is generally between the Johnston and Cruden DPLR predictions at 1.1 Torr, and is closer to Cruden mechanisms at 1.5 Torr. However, when comparing with the LASTA/Cantera simulations, all of the higher velocity cases show a good agreement with the Cruden mechanism. The LASTA/Cantera simulations, starting from a thermalized frozen condition, are unable to calculate the radiance right at the shock front where the gas is under thermal nonequilibrium. Results on shot 9 show the importance of taking into account the shock deceleration effect when determining which kinetic rate model is better suited to predict the measurements. In this case, the DPLR/NEQAIR results using the Johnston model lie on top of the LASTA/Cantera simulations using the Cruden model. While stagnation line similarity of the DPLR simulations to the 1D shock tube has been used in the past, the LASTA/Cantera calculations consider additional physical processes which should be more accurate than stagnation line comparisons. For this reason, the LASTA/Cantera simulations will be preferred over the DPLR results for the rest of the paper. One exception is the comparison of the radiance near the shock front, where the LASTA/Cantera simulations do not predict as well due to diffusion, thermal non-equilibrium and instrumental resolution. Deceleration effects should be minimal close to the shock front such that stagnation line similarity can still be assumed in this region.

For velocities below 2.6 km/s, the chemistry in the shock appears to be frozen in the time scale of the experiment, with a value up to 10% higher than the frozen condition predicted by CEA. The LASTA/Cantera simulations are very similar to the LASTA/Frozen simulations in all of these cases. The small differences in both DPLR results also indicate that the flow is frozen. The LASTA simulations overall improves the prediction of the measured radiance when compared to the frozen CEA solution, increasing further away from the shock front as observed in the test. The increase in radiance behind the shock front in the DPLR simulation is due to a different mechanism (increasing pressure due to stagnating flow) than the LASTA result and is not an expected shock tube phenomenon [28]. Figure 7 and 9 shows the spectral comparisons for the same shots as in Figures 6 and 8, measured from 1-3 cm behind the shock front. The results show that reacting flow results lie between frozen and equilibrium solutions, as expected. For the lower velocity shots, the comparison shows results to exceed the frozen result at all wavelengths.

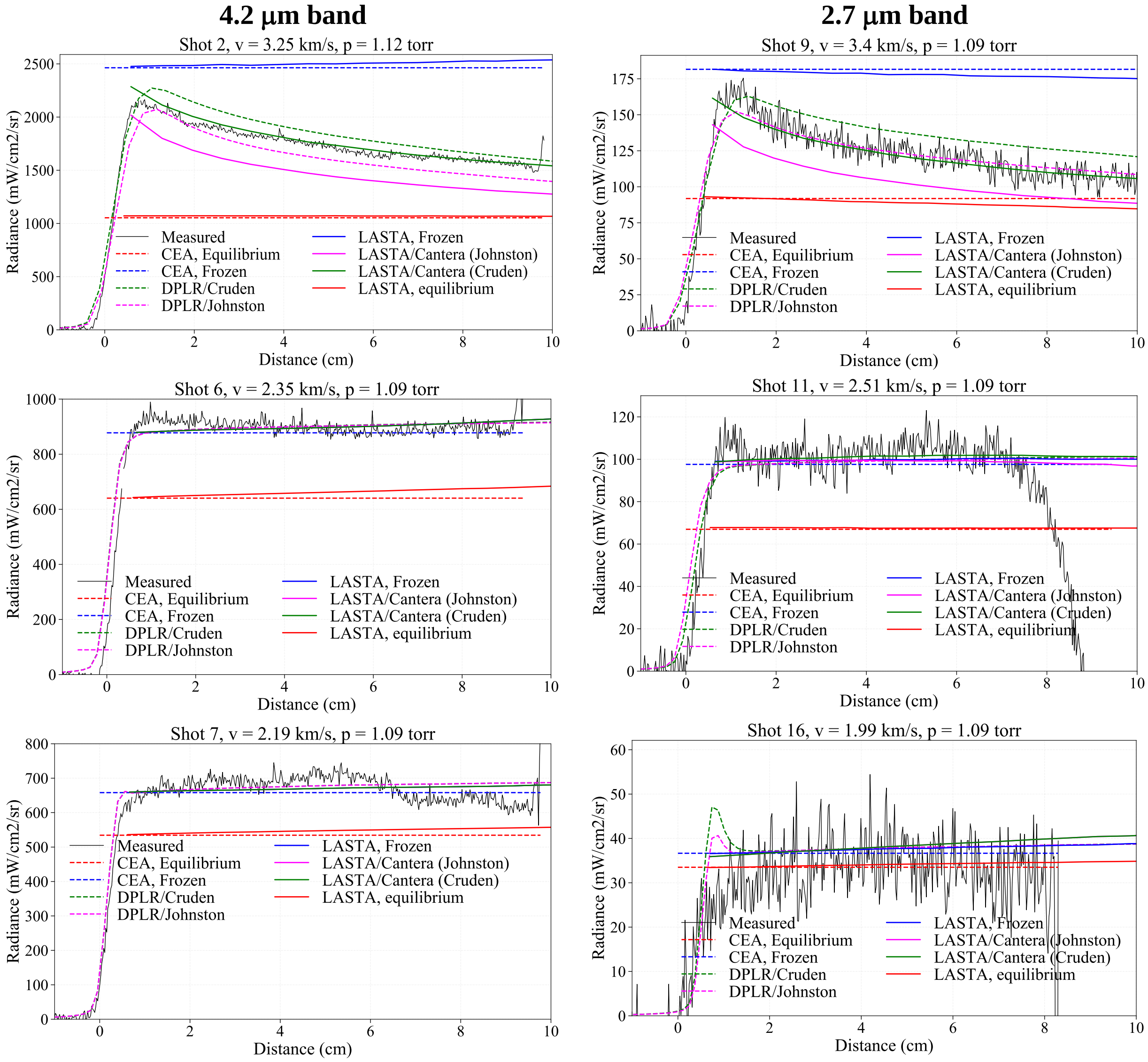

Figure 6: Comparison between measured (black) and computed integrated radiance profiles using CEA/NEQAIR, DPLR/NEQAIR or LASTA/NEQAIR predictions for different shots at 1.1 Torr. Left: for the 4.2 μm band. Right: for the 2.7 μm band

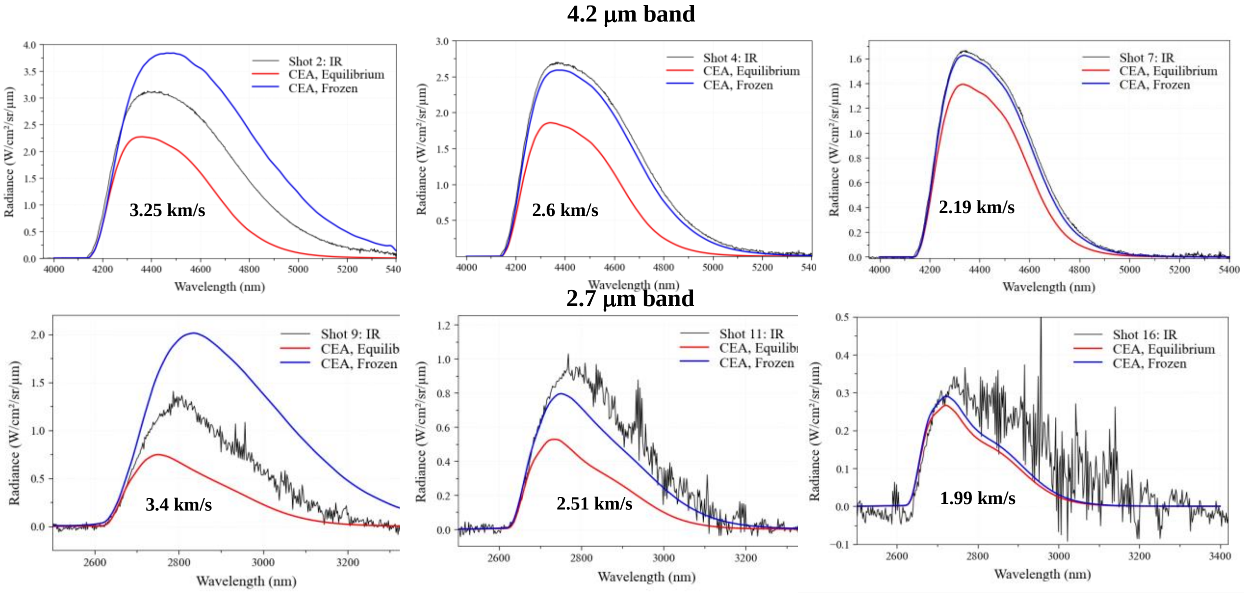

Figure 7: Comparison between measured spectra integrated over 1 cm starting around 2 cm from the shock front and CEA/NEQAIR predictions for different shots at 1.1 Torr

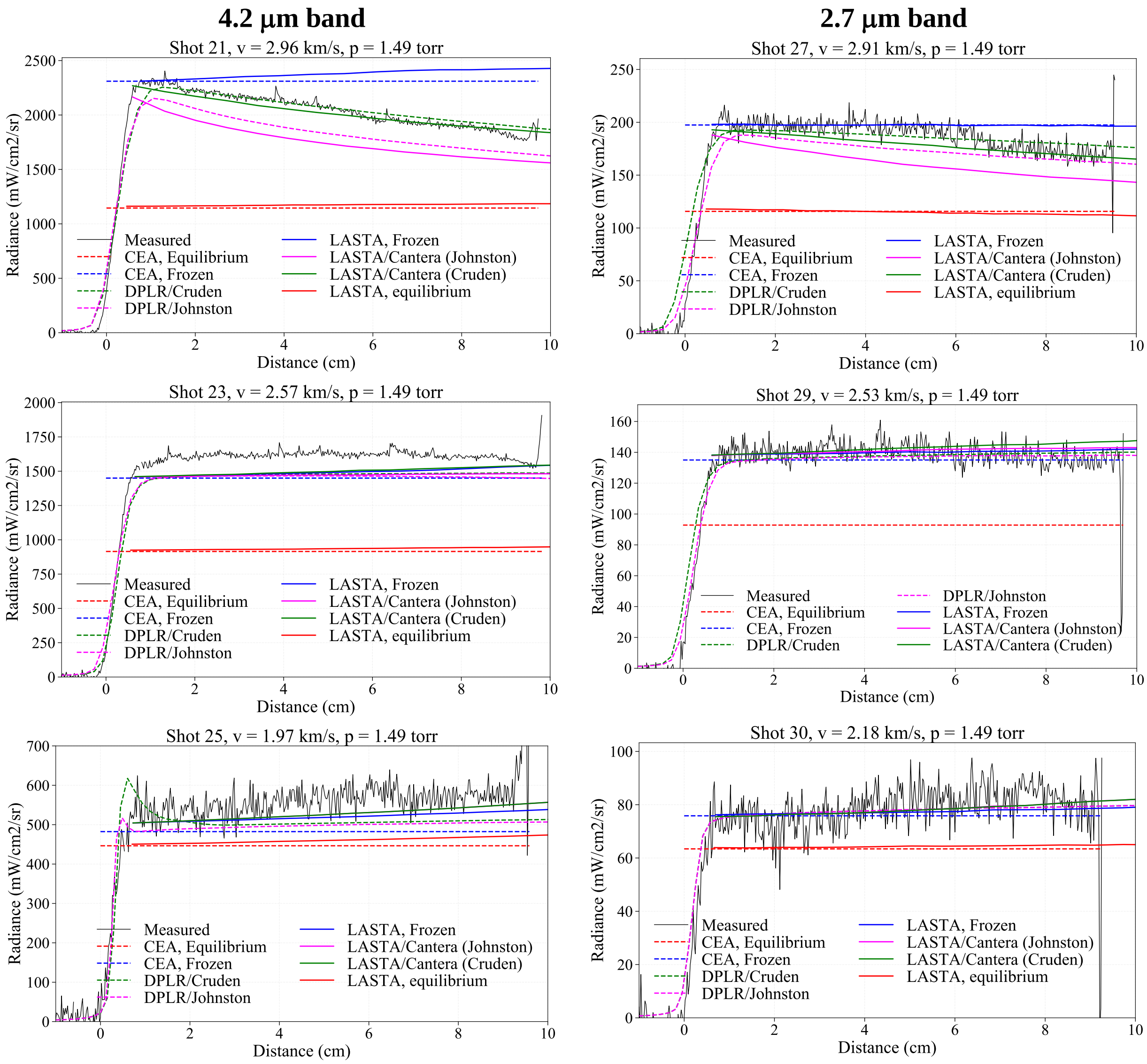

Figure 8: Comparison between measured (black) and computed integrated radiance profiles using CEA/NEQAIR, DPLR/NEQAIR or LASTA/NEQAIR predictions for different shots at 1.5 Torr. Top: for the 4.2 μm band. Bottom: for the 2.7 μm.

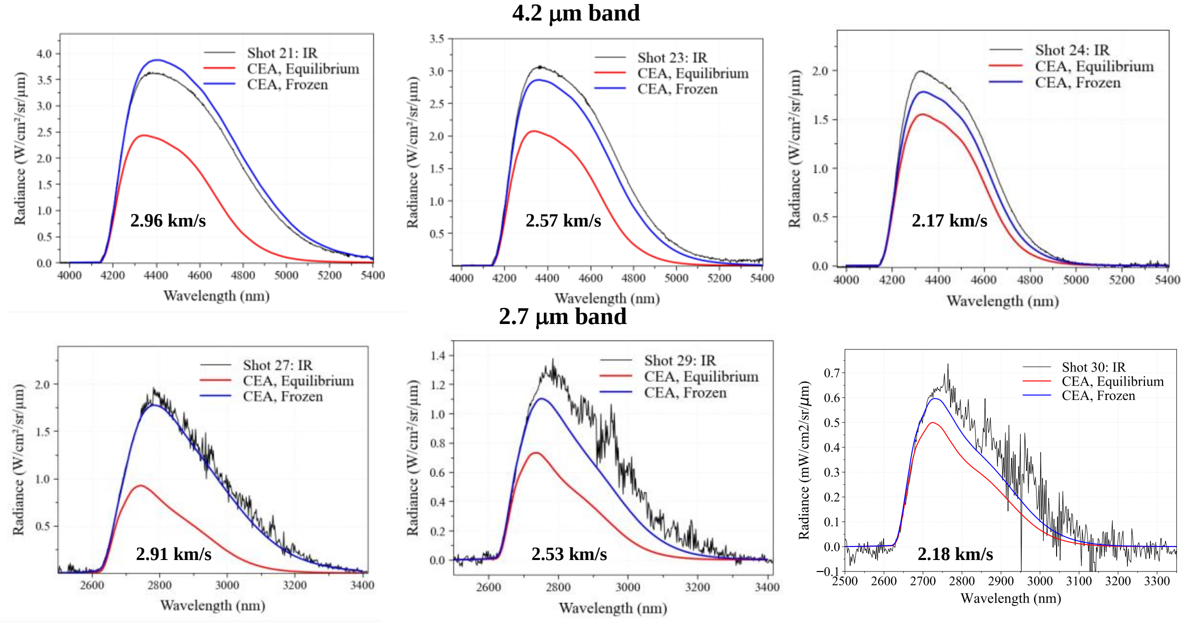

Figure 9: Comparison between measured spectra integrated over 1 cm starting around 2 cm from the shock front and CEA/NEQAIR predictions for different shots at 1.5 Torr

B. Comparison of the peak radiance

To compare the results from all shots performed during the test series, the peak radiance (i.e. radiance binned over ±2 cm around the shock front) at fill pressures of 1.1, 1.5 and 2.0 torr for both CO_2 bands are presented in Figure 10. The error bars are based on the noise level measured on the radiance profile (as seen in figs. 6 and 8) around a moving average value. Predicted values are taken from the DPLR/NEQAIR stagnation line solution since the region being measured is close to the shock front. At velocities below 2.7 km/s, the measured peak radiance is underpredicted by a maximum of 15% for both bands and all fill pressures. For velocities above 2.7 km/s, the measured radiance lies between the Cruden and Johnston model. The Cruden model agrees within the error of the measurement at all points in this regime, while the Johnston model agrees with some of the points. For 3.75 km/s, the highest velocity reported in this paper, a good agreement is observed between the measurement and the Cruden model. This is consistent with the results from a previous test series reported in

Ref. [29] which showed a better agreement between measurements and predictions using the Cruden model from velocity from 3.8 to 6.6 km/s.

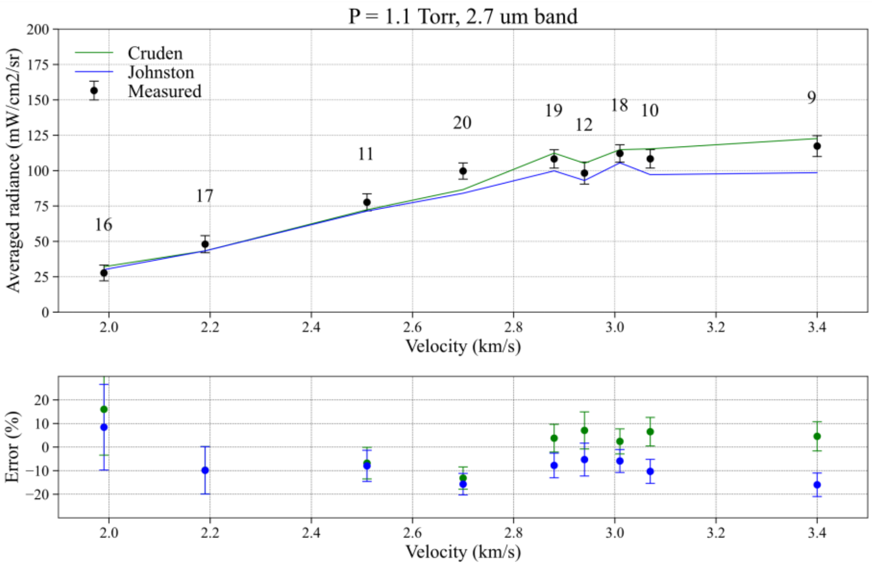

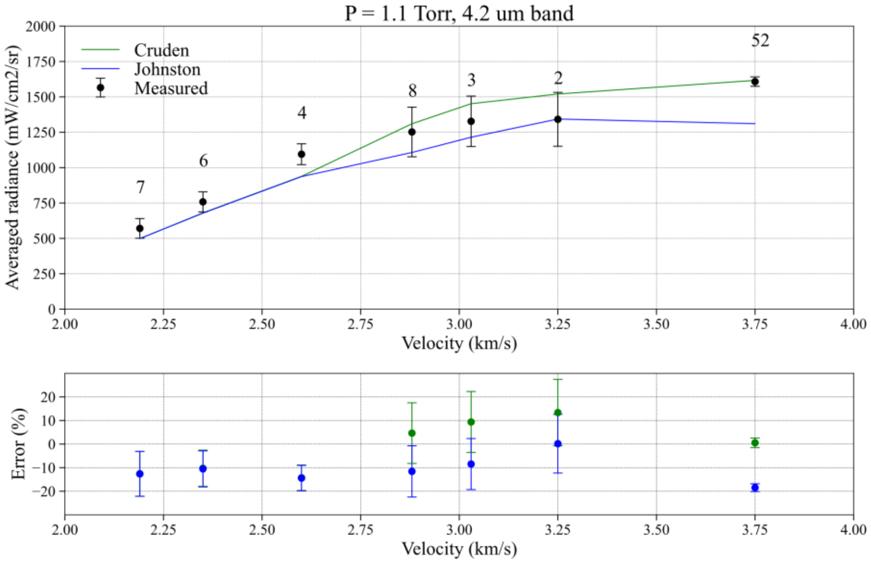

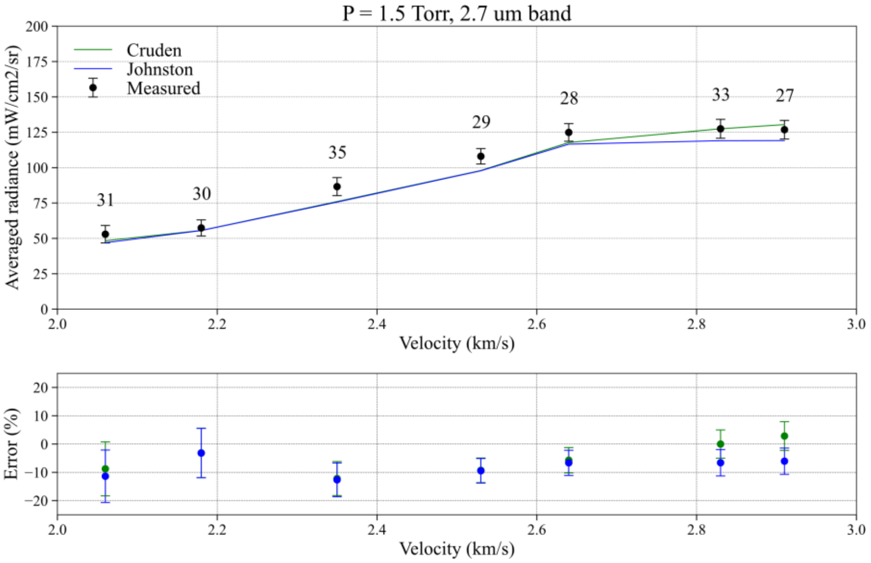
P = 1.5 Torr, 2.7 um band
Cruden
Johnston
Measured
Averaged radiance (mW/cm2/sr)
Velocity (km/s)
31
30
35
29
28
33
27
0
25
50
75
100
125
150
175
200
2.0
2.2
2.4
2.6
2.8
3.0
Error (%)
20
10
0
−10
−20
Velocity (km/s)

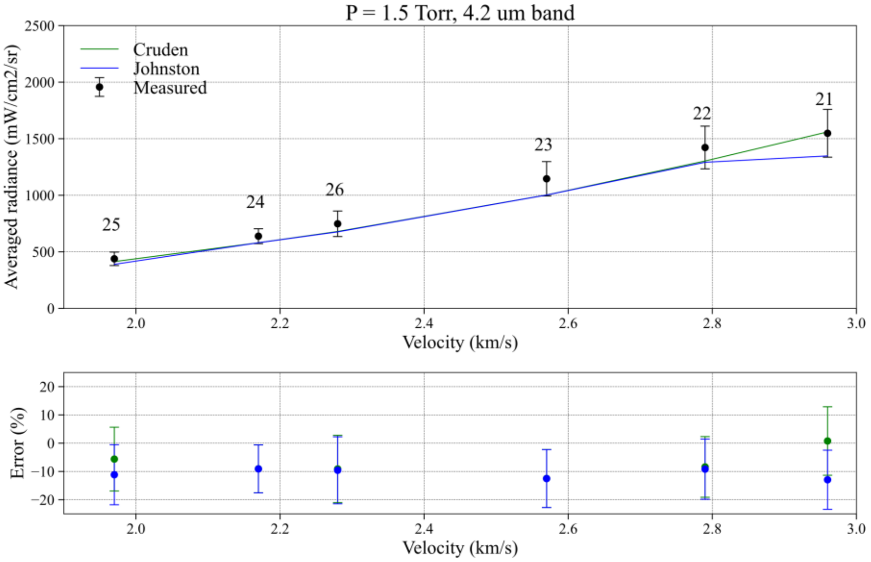
P = 1.5 Torr, 4.2 um band
Cruden
Johnston
Measured
Averaged radiance (mW/cm2/sr)
Velocity (km/s)
25
24
26
23
22
21
0
500
1000
1500
2000
2500
2.0
2.2
2.4
2.6
2.8
3.0
Error (%)
20
10
0
−10
−20
Velocity (km/s)

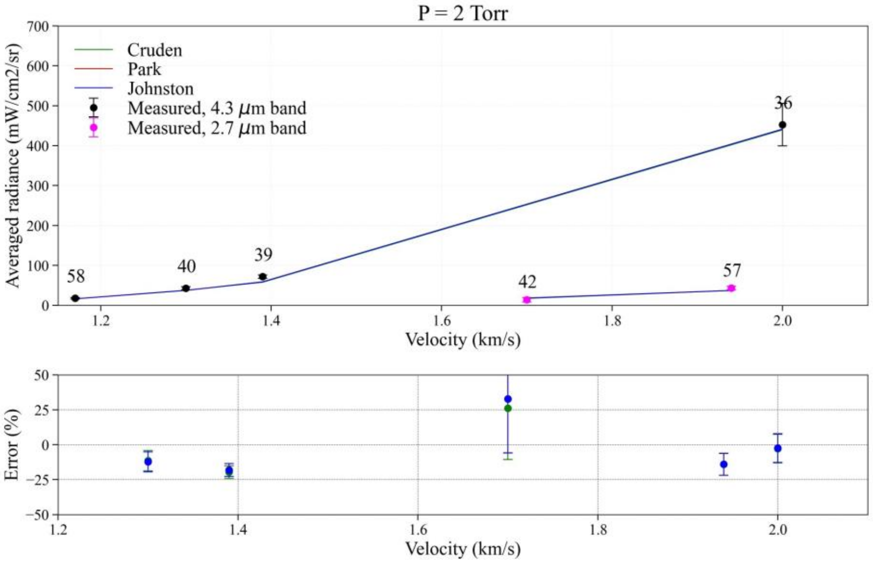

Figure 10: Comparison between measured and computed peak radiance (±2 cm from the shock front) for all fill pressure and both CO_2 bands

C. Comparison at larger distance from the shock front

For comparison relevant to backshell radiative heating, the evolution of the error predictions further away from the shock are analyzed as an indicator of the model accuracy. As an example, Figure 11 shows the same comparison made in Figure 10, but for an averaged radiance integrated over 0.25-0.35 ms particle time, which corresponds to the largest particle time available for every shot. To calculate the particle time, the velocity behind the shock wave is taken from CFD results (u_{CFD}) and used to convert the distance behind the shock front ($dx_{measured}$) to time, i.e. $t_{part} = \int (dx_{measured}/u_{CFD})$. The LASTA/Cantera results were used for this comparison, as discussed earlier. Frozen and equilibrium radiance values, using LASTA simulations, are shown for comparison. All models predict frozen chemistry for velocities below 2.7 km/s for all pressures, as discussed previously. Most of the measurements are in agreement with the frozen radiance computed by LASTA/NEQAIR, with the exception of the results for the 4.2 μm band at 1.5 Torr, where the radiance is underpredicted by 5 to 10%. For velocities above 2.7 km/s, the measurements are very well predicted by the Cruden mechanism, and underpredicted by about 10 to 15% by the Johnston mechanism. While not shown in the figure, the radiance predicted by the DPLR simulations are usually 5 to 10% higher than the LASTA/Cantera results at that time. Finally, the spike in equilibrium and frozen radiance observed for shot 12 is due to a higher shock deceleration measured during the experiment, and the measured radiance remains well predicted by the LASTA/Cruden simulation.

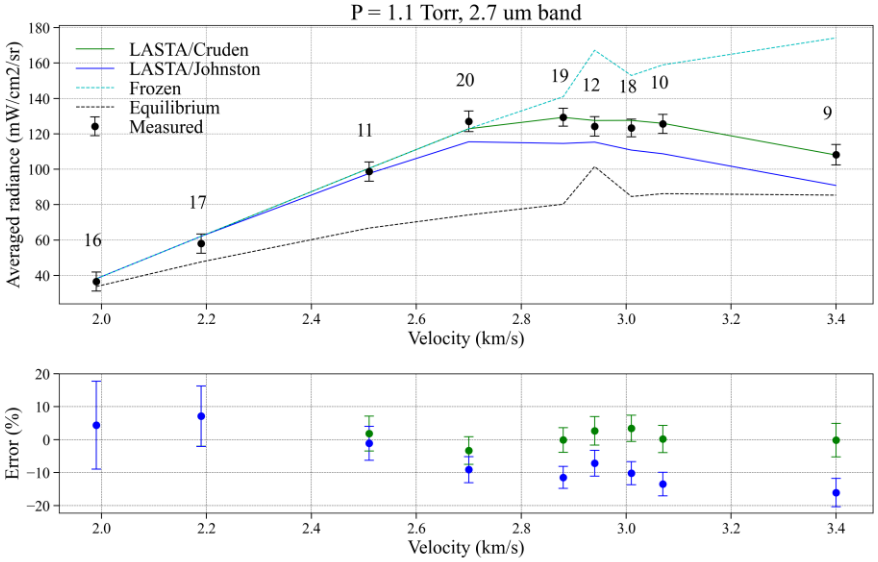

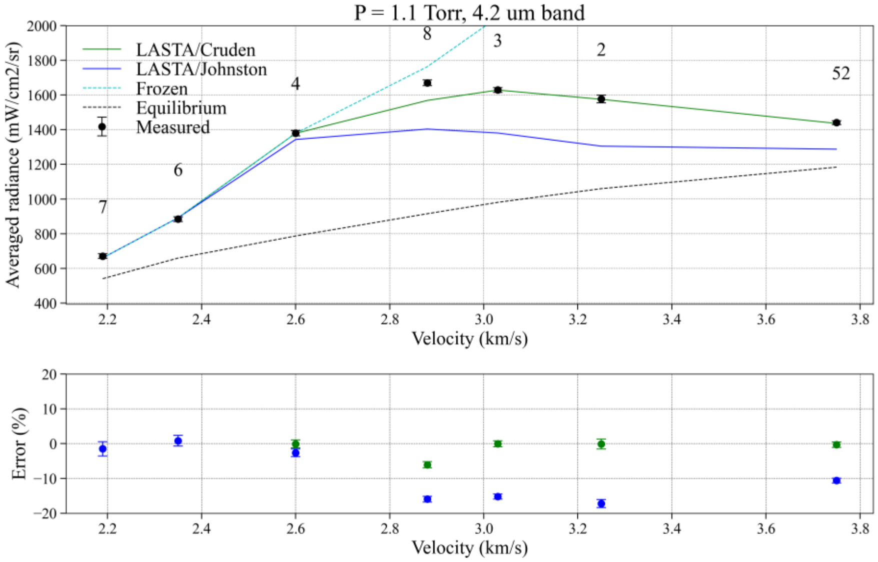

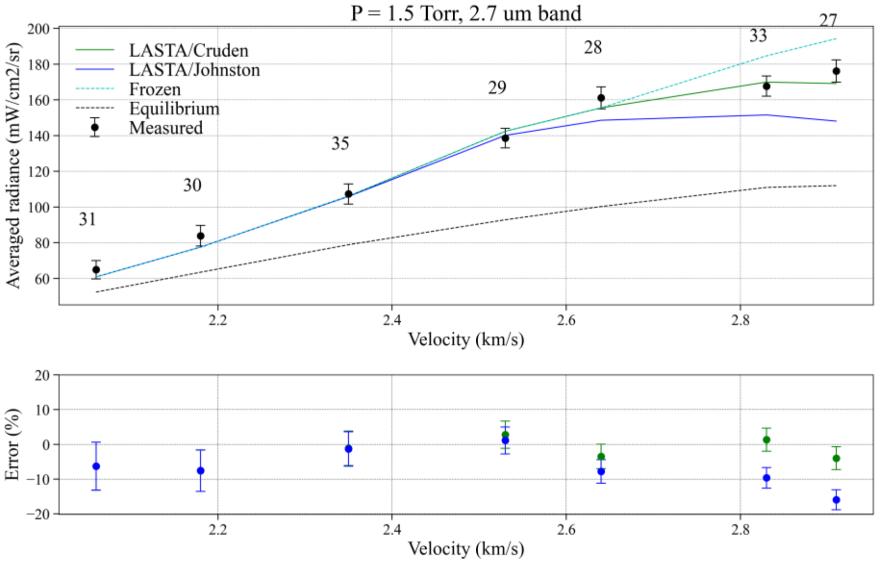
P = 1.5 Torr, 2.7 um band
LASTA/Cruden
LASTA/Johnston
Frozen
Equilibrium
Measured
Averaged radiance (mW/cm2/sr)
200
180
160
140
120
100
80
60
31
30
35
29
28
33
27
2.2
2.4
2.6
2.8
Velocity (km/s)
Error (%)
20
10
0
−10
−20
2.2
2.4
2.6
2.8
Velocity (km/s)

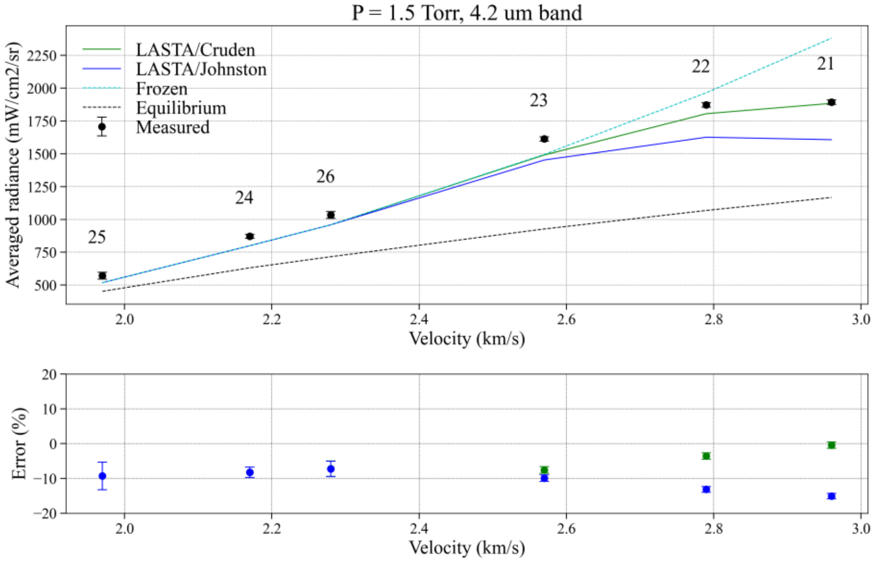
P = 1.5 Torr, 4.2 um band
LASTA/Cruden
LASTA/Johnston
Frozen
Equilibrium
Measured
Averaged radiance (mW/cm2/sr)
2250
2000
1750
1500
1250
1000
750
500
25
24
26
23
22
21
2.0
2.2
2.4
2.6
2.8
3.0
Velocity (km/s)
Error (%)
20
10
0
−10
−20
2.0
2.2
2.4
2.6
2.8
3.0
Velocity (km/s)

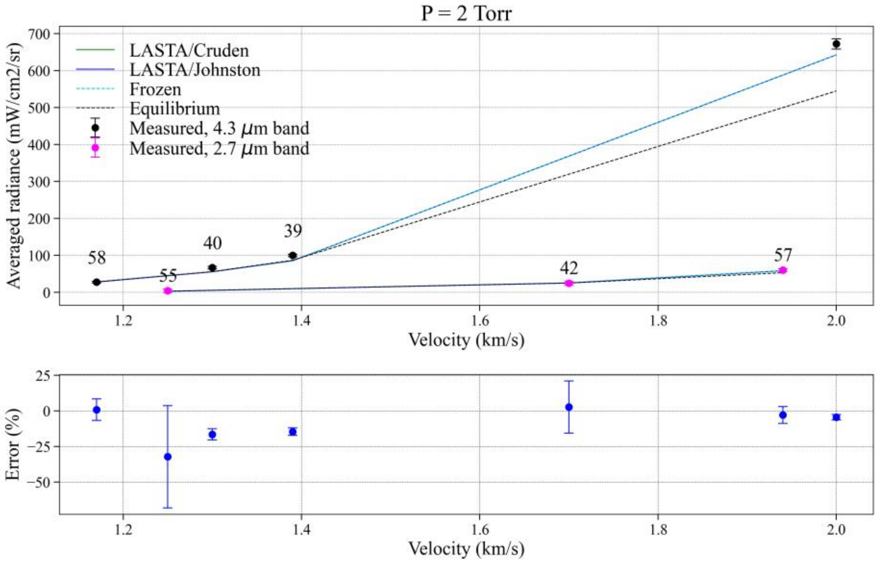

Figure 11: Comparison between measured and computed averaged radiance (over 250 to 350 μs in particle time, using the LASTA simulations) for all fill pressure and both CO_2 bands

As the chemistry appears frozen below 2.7 km/s, the higher velocity tests are the only ones able to differentiate reaction rate models. Based on Figure 14, these high velocity tests are important at the 1.1 Torr (t=92s) condition as they contribute more to the backshell radiative heating at this location. To assess the total uncertainties on the backshell, the evolution of the prediction error with particle time for the highest velocity shots performed in this test series are given in Figure 12 for a fill pressure of 1.1 and 1.5 Torr and velocities around 3.3 and 2.9 km/s, respectively. Both CO_2 bands are considered, and a total estimated error is given, which is computed using the relative intensity of both bands:

$$\varepsilon_{tot} = \frac{\varepsilon_{2.7\mu m}\Gamma_{2.7\mu m} + \varepsilon_{4.3\mu m}\Gamma_{4.3\,\mu m}}{\Gamma_{2.7\mu m} + \Gamma_{4.3\mu m}}$$

where Γ represents the cumulative radiance of a given band.

At 1.1 Torr, the error in the Cruden model is below 2% at all positions behind the shock except at 50 μs, which might be due at least in part to the inability of the LASTA/Cantera simulations to correctly predict the radiance at the shock front. On the other hand, the Johnston models start with a -5% error that decreases steadily to -15% at 100 μs and remain about constant at longer time. At 1.5 Torr, a similar observation is made for the Johnston model with an error starting around 0% and decreasing to a steady value around -15% after 100 μs, while the error with the Cruden model remains below 5% at all time points besides the first. To estimate the error in the model at the Mars2020 radiometer location, these profiles will be extrapolated to values from 1-10 ms in the next section.

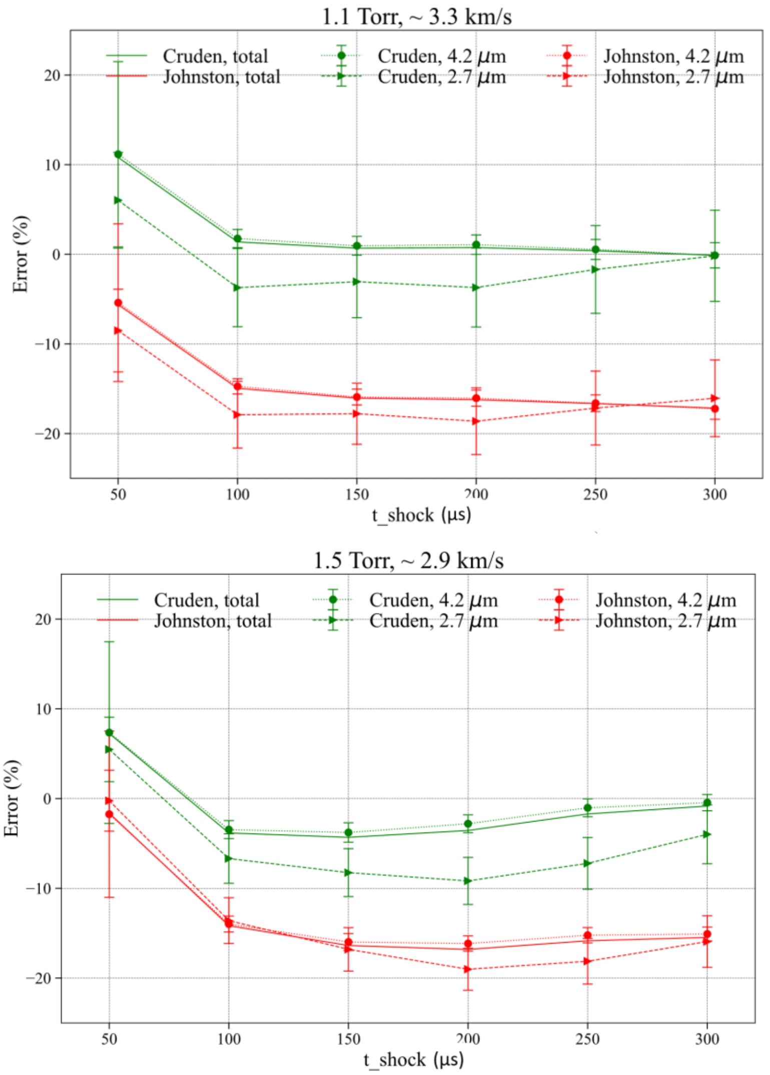

Figure 12: Evolution of the error between predicted and measured radiance as a function of particle time, for the three models considered.

Another quantity to consider is the relaxation time to equilibrium, after which models and experiments should predict the same radiance value. The characteristic relaxation time to equilibrium was obtained by fitting the radiance profiles with an exponential curve trending to the equilibrium value obtained by CEA, with results shown in Figure 13. Both measured and predicted profiles were fit the same way to ensure consistency in the comparison. Despite some scatter in the data, the curves show relative consistency as a function of velocity, with the characteristic relaxation time decreasing as the velocity increases. Comparison between shots at the same velocity for the two different pressures also show similar values, which might be expected for a relatively small change in pressure. Using the Cruden mechanism, the measured relaxation time obtained by fitting both bands shows a good agreement at 1.1 Torr, while being overestimated usually by 10%, and up to 40% for the highest velocity. On the other hand, the Johnston model consistently underpredicts the measured relaxation time by up to 40%. The relaxation time using the 2.7 μm band is consistently lower than that for the 4.2 μm band, for both experiments and simulations. For the range of data studied, the characteristic relaxation time is between 0.5 to 2 ms.

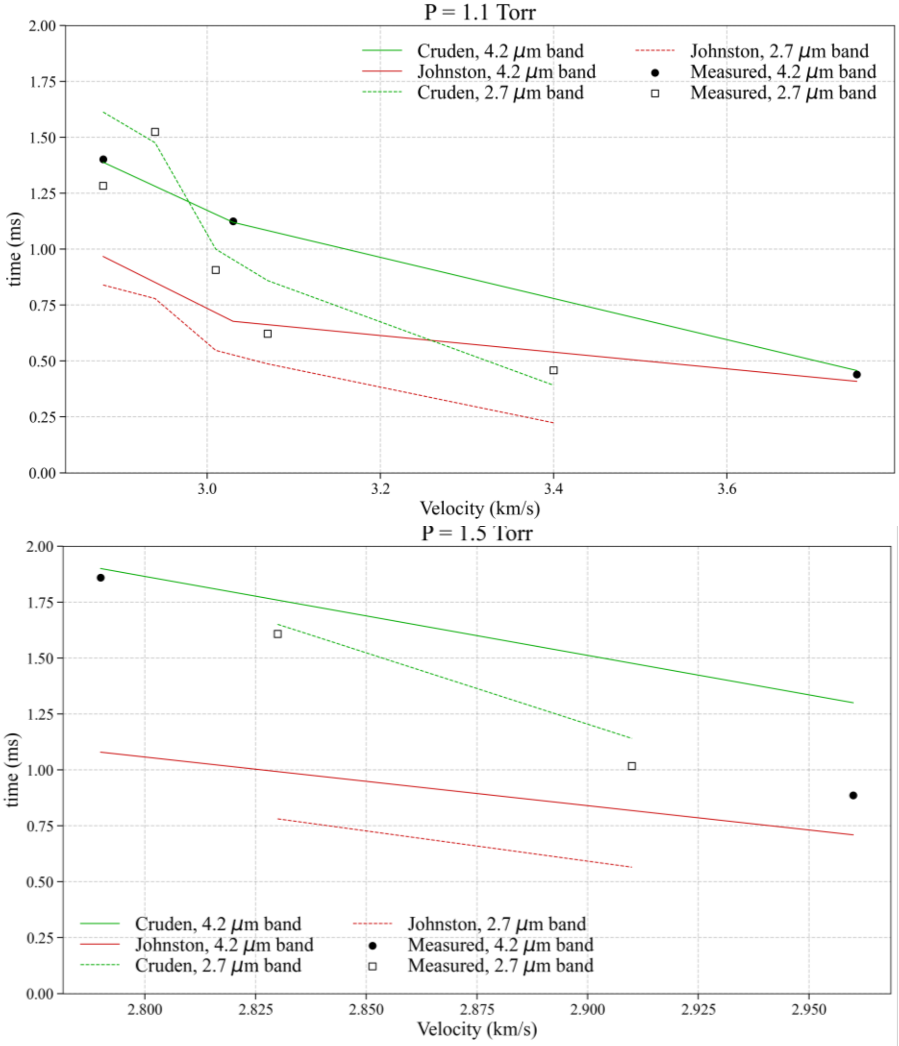

Figure 13: Estimated relaxation time to equilibrium based on the predicted (lines) and measured (points) radiance profiles for all shots above 2.7 km/s, for both CO_2 bands considered

D. Comparison with flight data

One of the primary goals of this test series is to validate the models used for radiative heating on the backshell using the shock tube informed bias and flowfield property binning methods [8, 30]. For a given point in the backshell, this method estimates where the gas emitting the radiation impacting the backshell originates from, which is then related to both normal shock velocity and particle time. The results are given as a fraction of the total heat flux $F_{bin,I,j}$ (with $\sum F_{bin,I,j} = 1$). This analysis was performed here for the Mars2020 entry trajectory at the locations corresponding to the heat flux and radiometer gauges shown in Figure 14. Two locations are presented on the lee and wind side corresponding to the heat flux gauge locations. Figure 14 also shows the radiative heating bin distributions for freestream pressures of 1.1 and 1.5 Torr. For the 1.1 Torr condition, most of the radiation measured during the entry is predicted to come from a shocked gas at 3 to 3.2 km/s, after travelling 1 to 8 ms from the shock front (in particle time) at the MTB08 location, and from 2.7 to 3 km/s, after travelling from 1 to 7 ms, at the MTB07 location. At 1.5 Torr, the relevant velocities are from 2.5 to 2.6 km/s and from 2.4 to 2.5 km/s and particle time has increased to be mostly between 3 to 12 ms and 2 to 10 ms at the MTB08 and MTB07 locations, respectively. Considering the case at 1.5 Torr and 2.5 km/s, the particle velocity behind the shock front is expected to be 230 m/s based on CEA calculations. The experiments only allowed measured radiation up to 10 cm from the shock front, i.e. a particle time around *400* μs. This value is typical of the maximum particle time for most shots. These times are lower than those indicated in Figure 14, which suggests they may be more relevant for positions closer on the backshell or at lower pressure where binary scaling can be applied [8]. Nevertheless, the measurements do give information about chemical relaxation rates and can be used to test the applicability of different reaction models at these conditions.

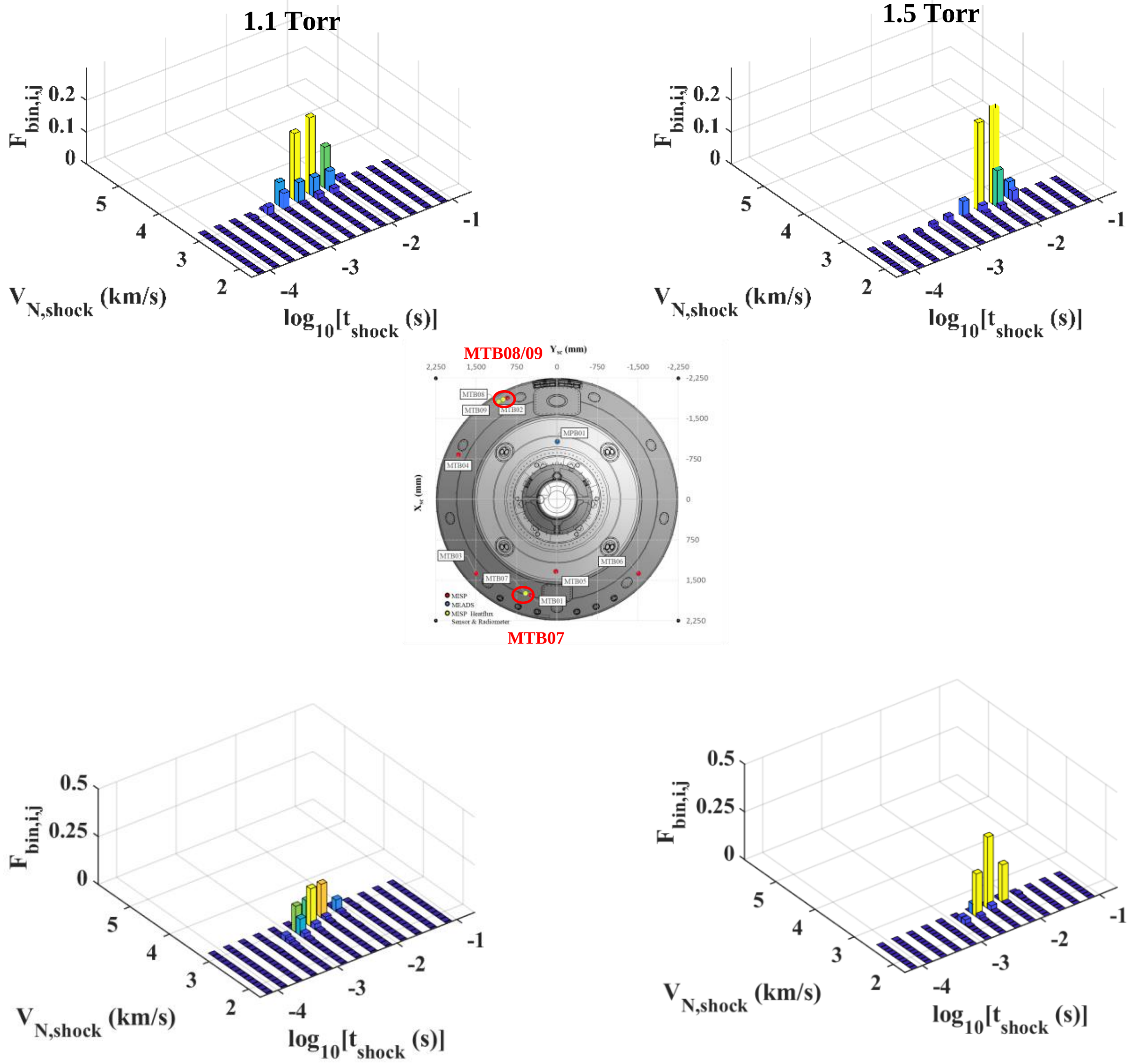

Figure 14: Radiative heating bin distributions for the surface point MTB07 (bottom) and MTB08/MTB09 (top) for the Mars2020 entry at a freestream pressure of 1.1 (left) and 1.5 Torr (right). The locations of the sensors are shown in the center.

For the 1.5 Torr case, most of the radiation measured by the MTB08/09 sensors originates from shock velocities between 2.5 to 2.6 km/s, and between 2.4 and 2.5 km/s at the MTB07 location. In the timescale of our experiments, the chemistry appears to be frozen in these conditions, so tests cannot be used to infer the prediction accuracy at the flight timescale. A shot at 2.5 km/s, 9 Torr was performed which, based on the test time and binary scaling, would provide an equivalent particle time of about 1 ms at 1.5 Torr. This test was also found to be frozen in the experimental measurement and by the Cruden model, though Johnston models predicted some reaction in this timescale. This may give some indication about the prediction accuracy but is not sufficient to quantitatively evaluate the accuracy of the flight predictions at t=101s.

For the 1.1 Torr case, the relaxation times are about 3x less than the particle time from which the gas radiation originates from. Figure 12 indicates the radiation might be underpredicted by up to 15% with the Johnston models while well predicted by the Cruden model. To estimate the error at flight scale, the exponential curve fits used to obtain relaxation time are extended out to 8 ms to be representative of the radiance measured at the MTB08 location, using velocities from 3 to 3.2 km/s. The error between the fitted predicted radiance curve and the measurements show a 5% underestimation using the Johnston mechanism, while the Cruden mechanism shows a near perfect agreement (+0.2% error). This is consistent with the difference between the radiance predicted by the two models in Figure 1 at 92 s (about 5%). The near perfect agreement was expected for the Cruden mechanism, as both the radiance at 300 μs and the relaxation time were well predicted (see Figs 11 and 13) at 1.1 Torr and 3.1 km/s. At the MTB07 location, the velocity range of interest is 2.7 km/s to 3 km/s. Using the same procedure with shots around 2.9 km/s, the total error between the measured and predicted radiance at the MTB07 location would be −8% and +0.5% with the Johnston and Cruden model, respectively. This is also consistent with the difference in radiance predicted by the two models at the MTB07 location (about 10%). The relative consistency in the disagreement between the two models from this method and the corresponding full vehicle predictions at both vehicle locations serves to validate the shock tube informed bias methodology. Overall, the Cruden model seems to better predict the radiation in the backshell region, although an extended analysis at different times in the trajectory needs to be made to confirm this observation.

E. Comparison with TDLAS measurements

Finally, the data obtained from OES were compared with the TDLAS measurements performed and presented in a companion paper [9]. In order to compare the temporally resolved TDLAS data with OES measurements, the measured radiance was binned over 0.5/1 cm intervals and fit to obtain post-shock number densities and temperatures. The binning interval is chosen as a compromise between having both good signal-to-noise ratio and spatial resolution. The fits are performed using the NEQAIR radiation code in a similar way as presented in Refs [26] [27]. The reported uncertainties in the emission data represent both systematic and random errors. The systematic error was estimated using the error of the fit parameters. For the random errors, a random and Gaussian artificial noise with standard deviation equal to that of the measured noise was added to each spectrum. These newly created spectra were then fit again. This was performed 10 times and an error equal to twice the standard deviation of the results was added to the error on the fit parameters. The total reported errors do not take into account uncertainties due to any shortcomings in the formulation of the radiation model. The reported center value for the temperatures and number densities correspond to the mean of all fitted spectra. TDLAS uncertainties consider the fit as well as the underlying linestrength model uncertainties. The temperature and CO_2 number density profiles obtained by OES and TDLAS measurements are compared in Figure 17 with LASTA/CEA and LASTA/Cantera predictions.

Temperature results from the emission and absorption techniques often showed a disagreement with TDLAS being 5 – 10% below temperatures measured from OES across the range of shock velocities. A few examples are shown in Figure 15. For the reacting case (shot 21), the OES measurements show a good agreement with the Cruden model, while the TDLAS measurements show a better agreement with the Johnston model. Despite this, both measurements mostly remain within their corresponding uncertainty bars. Some discrepancy may be attributed to boundary layer absorption biasing the TDLAS number density measurement low. A theoretical analysis based on Mirels' similar boundary layer profile [31] was performed as discussed in Ref. [9], and appears to reconcile the measurements at some conditions. However, a small gap persists between the measurements at other conditions, suggesting the boundary layer may not be fully accounted for. For the frozen cases, the TDLAS measurements are again slightly under the temperature profiles obtained from OES. This discrepancy is largely within the uncertainty of the two measurement techniques as TDLAS estimates a 4.1 - 6.6% uncertainty as shock velocity increases from 2 – 3 km/s and OES estimates the fitting uncertainty as 3.5%. The LASTA temperatures generally lie between the temperatures obtained with both methods but is closer to the OES temperatures. Other sources of discrepancy could include the possibility of a turbulent boundary layer resulting in a thicker cool gas region than is accounted for in the analysis or the possibility that a complex thermal non-equilibrium persists between the asymmetric stretch mode and the rotational energy mode of the gas. The OES temperature will be primarily sensitive to the asymmetric stretch temperature, while the LAS temperature reported here is sensitive to multiple energy modes (rotation, bending mode vibration and asymmetric stretch vibration). For more details about the LAS uncertainties, refer to the companion paper [9]. For all cases, the number density profiles measured by both LAS and OES are within the uncertainties of the measurements and agree with LASTA within the uncertainty. In the future, an updated line selection can be utilized in the LAS technique to reduce uncertainty and an experimental investigation of the boundary layer can be conducted.

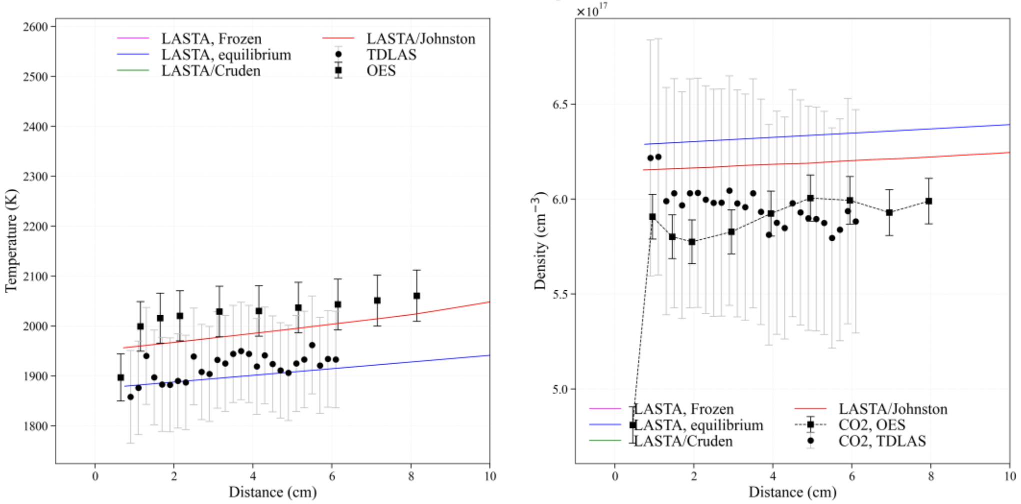
Shot 36, v = 2.0 km/s, p = 1.99 torr

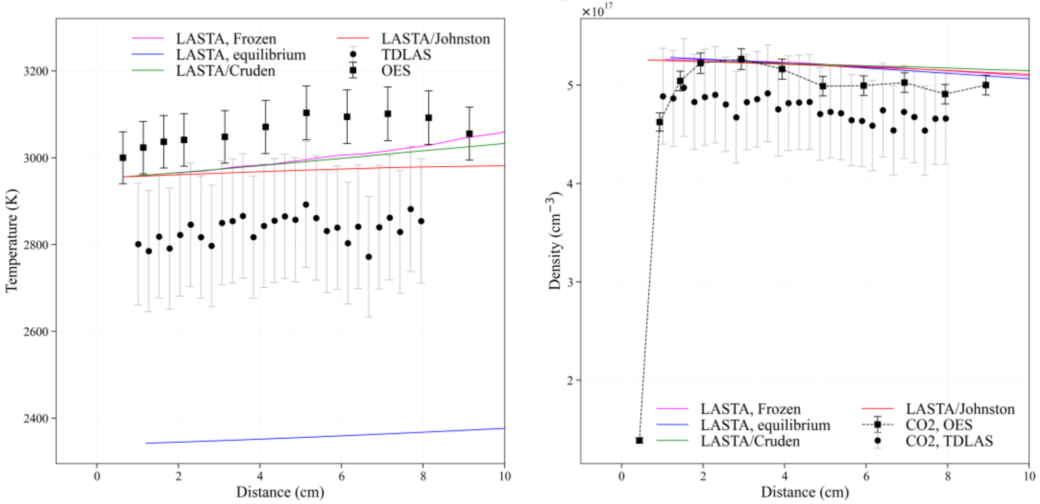
Shot 23, v = 2.57 km/s, p = 1.49 torr

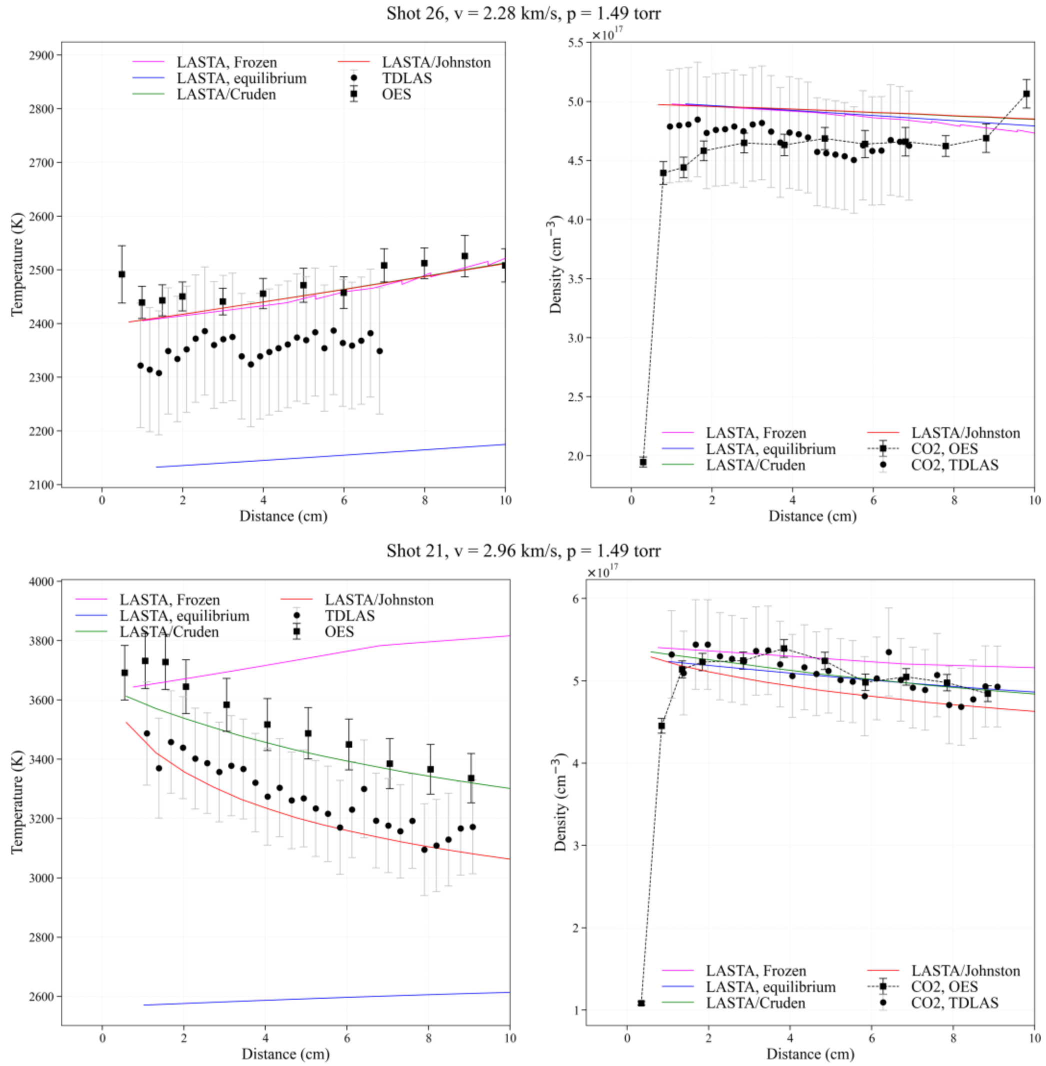

Figure 15: Comparison between temperature and CO₂ number density profiles measured by OES and TDLAS and predicted by LASTA simulations.

Finally, to compare all the measurements obtained by OES and TDLAS and the simulations, a radiance profile was computed using NEQAIR and the temperatures and number densities obtained with TDLAS. A comparison of the radiance profiles is presented in Figure 16, representing the same results as in Figure 6 with the radiance computed from the TDLAS measurements overlaid on the plot. The uncertainty on the radiance obtained from TDLAS measurements are higher than the noise observed with OES, which can be expected, as OES is a direct measurement of radiance. Overall, a good agreement is observed between the OES and TDLAS radiance. For the reacting cases, the radiance profiles obtained from the TDLAS measurements also show a better agreement with the Cruden mechanism, as previously observed in section IV.

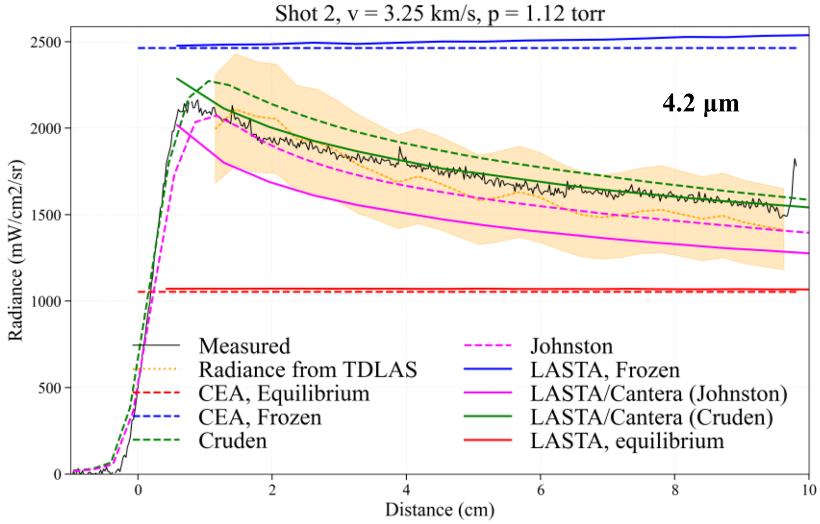

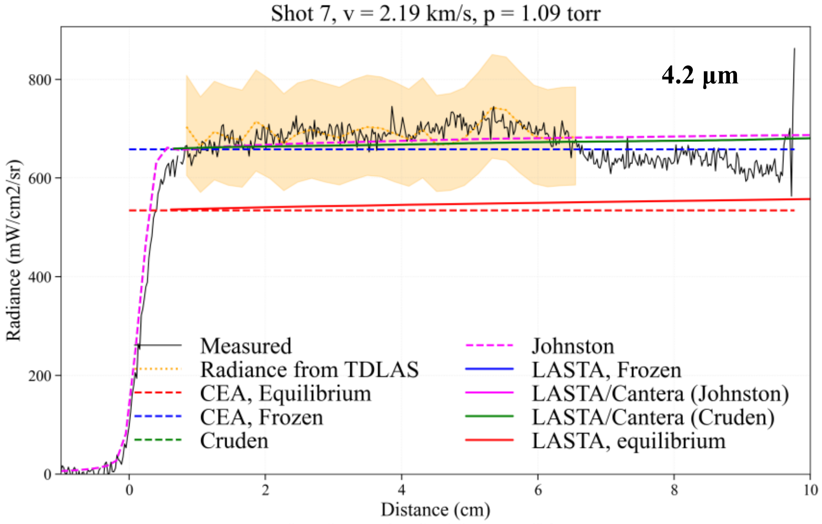

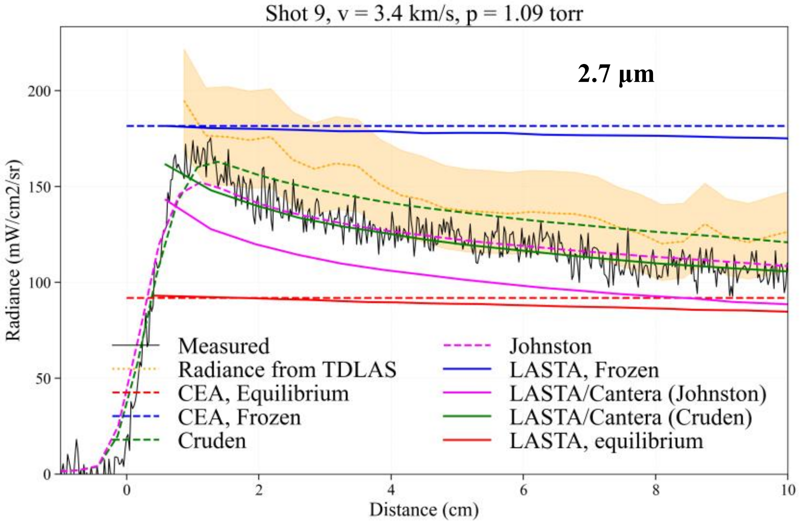

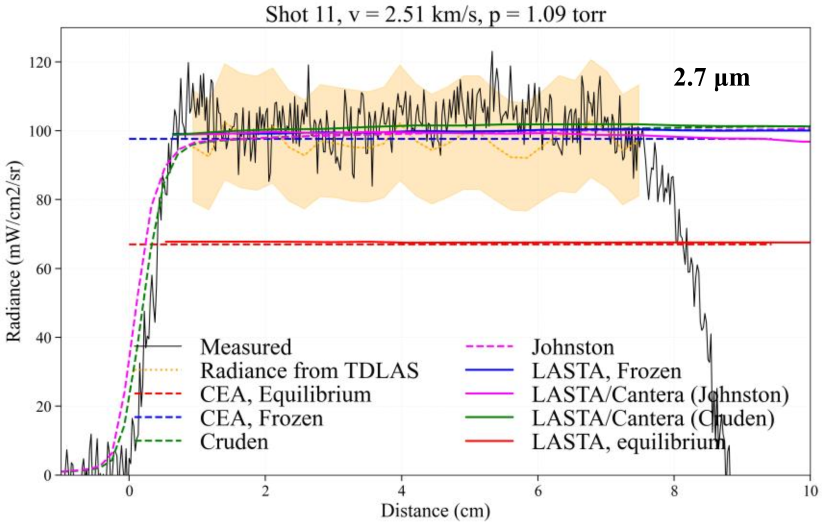

Figure 16: Radiance profile comparison between measurements using OES and TDLAS, and simulations using CEA/NEQAIR, DPLR/NEQAIR or LASTA/NEQAIR for different shots at 1.1 Torr.

As a summary of all measurements, the radiance profiles were then averaged over 50 to 300 µs from the shock front – in a similar way than previously done in Figs. 10 and 11 – to take into account most of the measured profiles, while ignoring nonequilibrium effects near the shock front. Results are presented in Figure 17. The TDLAS uncertainty bars are generally larger than the OES ones, as noted above. Overall, a good agreement between the two measurements is observed for the 2.7 µm band, while the 4.2 µm band sometimes shows some discrepancy. For the 2.7 µm band, at 1.1 Torr, the agreement between the two measurements is good below 2.7 km/s, with the TDLAS radiance within the uncertainty of the OES data. At 1.5 Torr, the 2.7 µm band agrees within the uncertainty. The discrepancy observed between the measurements for the 4.2 µm band comes from the difference in the temperature, leading to a lower radiance in the tail of the band. This discrepancy is not observed for the 2.7 µm band as only the wavelengths near the bandhead are considered (see Section III). While the TDLAS temperature profile presented in Figure 15 showed a better agreement with the Johnston model, Figure 17 overall shows a better agreement between the TDLAS radiance and the predicted radiance using the Cruden mechanism.

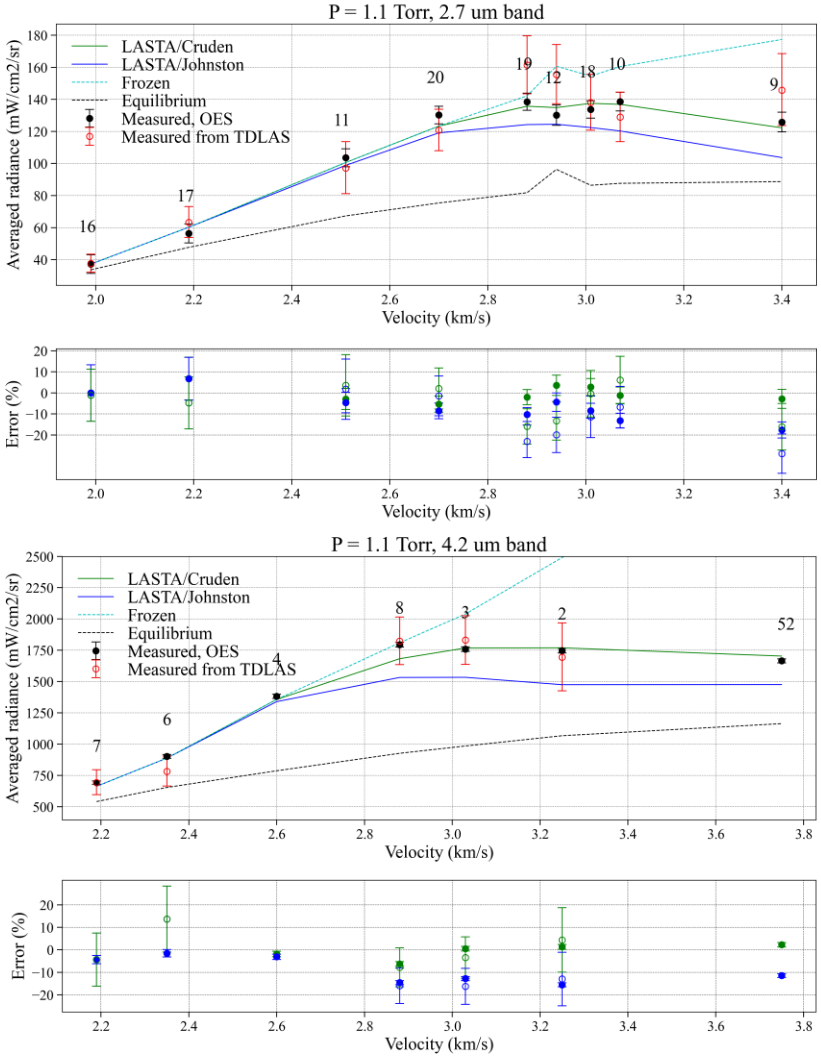

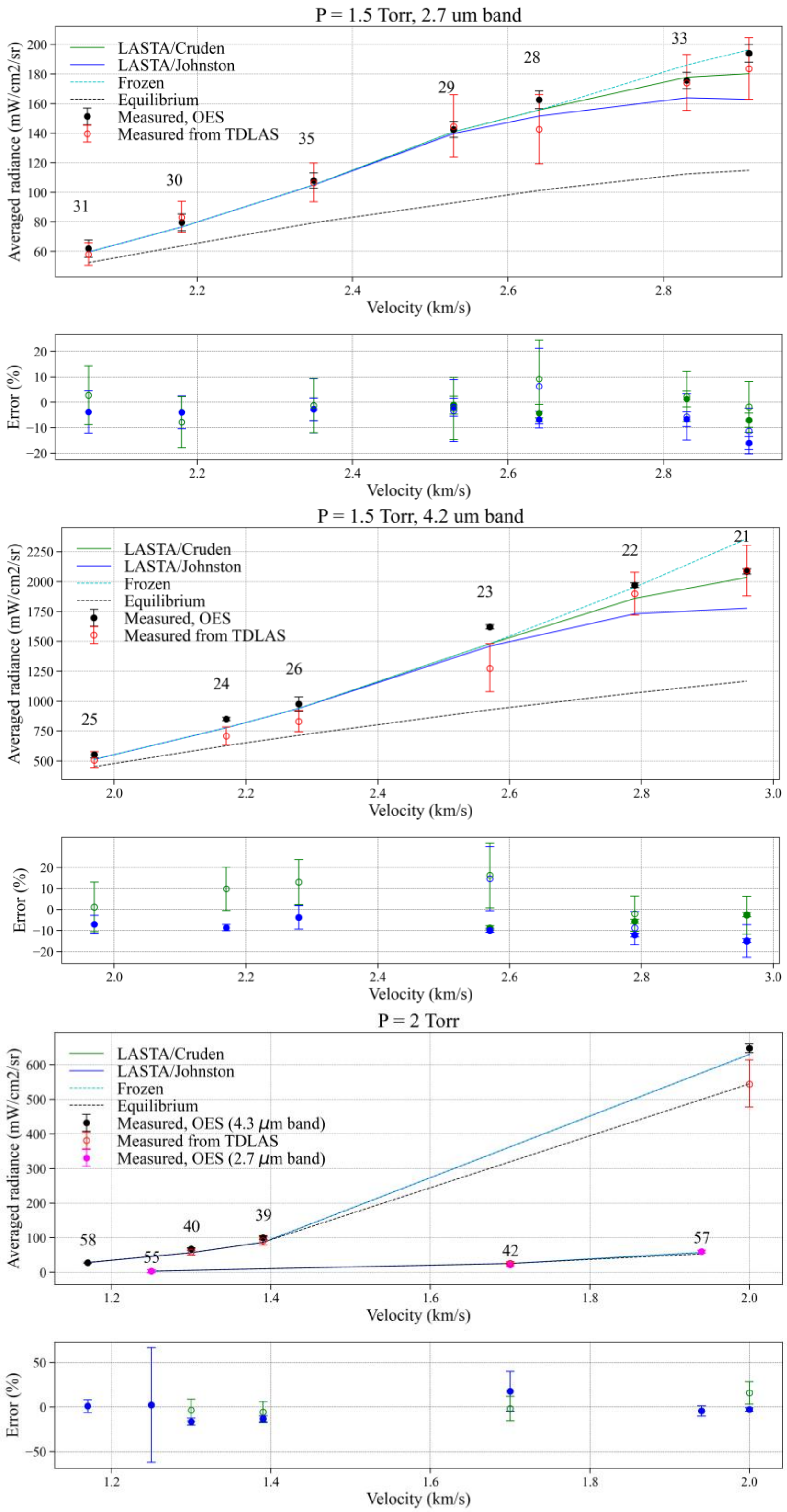

Figure 17: Comparison between OES, TDLAS and computed radiance averaged over 50 to 300 μs for all fill pressure and both CO_2 bands

V. Conclusions

A test series was performed in the EAST facility aiming to reconstruct the backshell radiation measured by the MEDLI2 sensors during the Mars2020 entry. OES measurements were performed and compared to CFD simulations using two different kinetic models, referred to as Johnston and Cruden. Simulations using the LASTA code were also performed to take into account shock deceleration effects, and coupled with the Cantera solver using the same two kinetic rate models. The LASTA/Cantera simulations were found to give more consistent results with data and are believed to be a better approach to modelling the shock tube than the CFD simulations. The Cruden model predicts slower chemistry than the Johnston model due to a lower CO_2 dissociation rate. The chemistry appears to be frozen below 2.7 km/s for all models and in the experiment. For those cases, the measured radiance was found to be higher than the frozen radiance computed using CEA/NEQAIR. The LASTA simulations improved the agreement with the measurements, but an underprediction up to 5-10% was still observed in some cases. At higher velocity, the measured peak radiance lay between the different models, with the Johnston models underpredicting the radiation by about 10%, while the Cruden model overpredicted it by up to 7%, but giving better agreement in many cases. However, 300 µs behind the shock front, a good agreement was observed between the Cruden model and the measurements while the Johnston model tended to underpredict the radiance by 10-15%.

For backshell radiation, particularly at the radiometer location, most of the gas emitting radiation to backshell will have to travel more than 1 and 3 ms from the shock front at the test conditions of 1.1 and 1.5 Torr, respectively. At 1.1 Torr, taking into account the relaxation time to equilibrium, the prediction is expected to be between 5 - 8% low using the Johnston model, while a near perfect (within 0.5 %) prediction is expected using the Cruden model at the heat flux gauge locations. At 1.5 Torr, most of the radiation is expected to come from shock velocities between 2.1 to 2.6 km/s which were found to be frozen in the timescale of the experiment, and uncertainty on the real flight measurement could not be determined.

Comparison with simultaneous LAS measurements were also performed. Temperatures inferred from OES were found to be close to the temperature measured by LAS but consistently higher, with up to 10% discrepancy. While boundary layer absorption reconciled some of the differences between the two techniques [9], a discrepancy was still observed, suggesting that this effect may not be fully taken into account. On the other hand, CO_2 number density profiles measured by both techniques showed a good agreement for all cases studied. Radiance profiles were inferred from the TDLAS measurements and compared with the OES measurements and predictions for all cases. While some difference between the two techniques were observed for the 4.2 μm band, a good agreement was observed for the 2.7 μm band. The radiance inferred from the TDLAS measurements was also found to be closer to the predictions using the Cruden mechanism, thus confirming that this model seems better suited to predict radiation in the backshell region.

Appendix A : Summary of all shots performed with useable data. The spectrometer settings are changed to measure both 4.2 and 2.7 μm CO_2 bands.

Shot number	Velocity (km/s)	Fill pressure (Torr)	CO_2 band measured (μm)
2	3.25	1.1	4.2
3	3.03	1.1	4.2
4	2.60	1.1	4.2
6	2.35	1.1	4.2
7	2.19	1.1	4.2
8	2.88	1.1	4.2
9	3.40	1.1	2.7
10	3.07	1.1	2.7
11	2.51	1.1	2.7
12	2.94	1.1	2.7
16	1.99	1.1	2.7
17	2.19	1.1	2.7
18	3.01	1.1	2.7
19	2.88	1.1	2.7
20	2.70	1.1	2.7
21	2.96	1.5	4.2

22	2.79	1.5	4.2
23	2.57	1.5	4.2
24	2.17	1.5	4.2
25	1.97	1.5	4.2
26	2.28	1.5	4.2
27	2.91	1.5	2.7
28	2.64	1.5	2.7
29	2.53	1.5	2.7
30	2.18	1.5	2.7
31	2.06	1.5	2.7
32	2.64	1.5	2.7
33	2.83	1.5	2.7
34	1.85	1.5	2.7
35	2.35	1.5	2.7
36	2.00	2.0	4.2
39	1.39	2.0	4.2
40	1.30	2.0	4.2
42	1.70	2.0	2.7
46	1.96	0.5	4.2
52	3.75	1.1	4.2
54	2.49	8.8	4.2
55	1.25	1.9	4.2
57	1.94	1.9	4.2
58	1.17	2.0	4.2
59	2.68	8.8	4.2

References

[1] C. Y. Tang, D. K. Prabhu, H. Alpert and B. A. Cruden, "MEDLI2: MISP Inferred Aerothermal Environment and Flow Transition Assessment," *AIAA SCITECH 2022 Forum,* no. AIAA 2022-0552, 2022.

[2] T. R. White, M. Mahzari, M. A. Ruth, C. Y. Tang, C. D. Karlgaard, H. Alpert, H. S. Wright and C. Kuhl, "Mars Entry Instrumentation Flight Data and Mars 2020 Entry Environments," *AIAA SCITECH 2022 Forum,* no. AIAA 2022-0011, 2022.

[3] R. A. Miller, C. Y. Tang, T. R. White and B. A. Cruden, "MEDLI2: MISP Measured Aftbody Aerothermal Environments," *AIAA SCITECH 2022 Forum,* no. AIAA 2022-0551, 2022.

[4] B. A. Cruden, D. K. Prabhu, A. Borner, J. Meurisse, J. Thornton and G. Bellas-Chatzigeorgis, "Measurement and Characterization of Mid-wave Infrared Radiation in CO2 Shocks," *Assessment of the Fluid Dynamics Boundary Condition in Ablating or Blowing Flows,* Vols. AIAA 2023-3614, 2023.

[5] C. O. Johnston and B. Kleb, "Uncertainty Analysis of Air Radiation for Lunar-Return Shock Layers," *Journal of Spacecraft and Rockets,* vol. 49, no. 3, pp. 425-434, 2012.

[6] A. M. Brandis, T. R. White, D. Sanders and J. Hill, "Simulation of the Schiaparelli Entry and Comparison to Aerothermal Flight Data," *AIAA Aviation 2019 Forum,* no. AIAA 2019-3260, 2019.

[7] B. A. Cruden, A. M. Brandis, T. R. White, M. Mahzari and D. Bose, "Radiative Heating During Mars Science Laboratory Entry: Simulation, Ground Test, and Flight," *Journal of Thermophysics and Heat Transfer,* vol. 30, no. 3, pp. 642-650, 2016.

[8] C. O. Johnston, "Evaluating Shock-Tube Informed Biases for Shock-Layer Radiative Heating Simulations," *Journal of Thermophysics and Heat Transfer,* vol. 35, no. 2, pp. 349-361, 2020.

[9] C. Jelloian, N. Minesi, R. M. Spearrin, A. Tibere-Inglesse, M. E. McDonald and B. A. Cruden, "Examination of Mars2020 shock-layer conditions via infrared laser absorption spectroscopy of CO2 and CO," *2023 AIAA SciTech forum, National Harbor, MD,* 2023.

[10] B. Cruden, R. Martinez, J. Grinstead and J. Olejniczak, "Simultaneous Vacuum-Ultraviolet Through Near-IR Absolute Radiation Measurement with Spatiotemporal Resolution in An Electric Arc Shock Tube," *41st AIAA Thermophysics Conference,* Vols. AIAA 2009-4240, AIAA, San Antonio, TX, 2009.

[11] S. P. Sharma and C. Park, "Operating Characteristics of a 60- and 10-cm Electric Arc-Driven Shock Tube-Part 11: The Driven Section," *Journal of Thermophysics and Heat Transfer,* vol. 4, no. 3, pp. 266-272, 1990.

[12] M. G. Trainer, T. H. McConnochie, H. B. Franz, S. K. Atreya, P. G. Conrad, F. Lefèvre, P. R. Mahaffy, C. A. Malespin, H. L. K. Manning, J. Martin-Torres, G. M. Martinez, C. P. McKay, R. Navarro-Gonzales, A. Vicente-Retortillo, C. R. Webster and M. P. Zorzano, "Seasonal Variations in Atmospheric Composition as Measured in Gale Crater, Mars," *Journal of Geophysical Research: Planets,* vol. 124, no. 11, pp. 3000-3024, 2019.

[13] P. R. Mahaffy, C. R. Webster, S. K. Atreya, H. Franz, M. Wong, P. G. Conrad, D. Harpold, J. J. Jones, L. A. Leshin, H. Manning, T. Owen, R. O. Pepin, S. Squyres, M. Trainer and M. S. L. S. Team, "Abundance and isotopic composition of gases in the martian atmosphere from the Curiosity rover," *Science,* vol. 341, no. 6143, pp. 263-6, 2013.

[14] A. M. Brandis, C. O. Johnston, B. A. Cruden and D. K. Prabhu, "Investigation of Nonequilibrium Radiation for Mars Entry," *51st AIAA Aerospace Sciences Meeting including the New Horizons Forum and Aerospace Exposition, Aerospace Sciences Meetings,* no. AIAA 2013-1055, 2013.

[15] B. A. Cruden and A. M. Brandis, "Measurement and Prediction of Radiative Non-equilibrium for Air Shocks Between 7-9 km/s," *American Institute of Aeronautics and Astronautics,* no. AIAA 2017-4535, 2017.

[16] M. J. Wright and D. Bose, "Data-Parallel Line Relaxation Method for the Navier-Stokes Equations," *AIAA Journal,* vol. 36, no. 9, pp. 1603-1609, 1998.

[17] B. A. Cruden, A. M. Brandis and D. K. Prabhu, "Compositional Dependence of Radiance in CO2/N2/Ar Systems," *44th AIAA Thermophysics Conference,* no. AIAA 2013-2502, 2013.

[18] C. Park, J. T. Howe, R. L. Jaffe and G. V. Candler, "Review of chemical-kinetic problems of future NASA missions, II: Mars entries," *Journal of Thermophysics and Heat transfer,* vol. 8, pp. 9-22, 1994.

[19] N. A. Ebrahim and R. J. Sandeman, "Interferometric studies of carbon dioxide dissociation in a free-piston shock tube," *The Journal of Chemical Physics,* vol. 65, no. 9, pp. 3446-3453, 1976.

[20] J. Clarke, M. McGilvray and L. Di Mare, "Numerical simulation of a shock tube in thermochemical non-equilibrium," in *AIAA SciTech conference,* 2023.

[21] A. M. Brandis, B. A. Cruden, D. Prabhu, D. Bose, M. McGilvray and R. Morgan, "Analysis of Air Radiation Measurements Obtained in the EAST and X2 Shocktube Facilities," *10th AIAA/ASME Joint Thermophysics and Heat Transfer Conference,* no. AIAA 2010-4510, 2010.

[22] P. L. Collen, M. Satchell, L. Di Mare and M. McGilvray, "The influence of shock speed variation on radiation and thermochemistry experiments in shock tubes," *Journal of Fluid Mechanics,* vol. 948, p. A51, 2022.

[23] M. Satchell, L. Di Mare and M. McGilvray, "Flow Nonuniformities Behind Accelerating and Decelerating Shock Waves in Shock Tubes," *AIAA Journal,* vol. 60, no. 3, pp. 1537-1548, 2021.

[24] M. Satchell, M. McGilvray and L. Di Mare , "Analytical Method of Evaluating Nonuniformities in Shock Tube Flows: Theory and Development," *AIAA Journal,* vol. 20, no. 2, pp. 654-668, 2021.

[25] P. L. Collen, M. Satchell, L. di Mare and M. McGilvray, "Analysis of Shock Deceleration Effects on Radiation Experiments in the NASA Electric Arc Shock Tube," *AIAA SCITECH 2022 Forum,* no. 2022-0267, 2022.

[26] D. G. Goodwin, H. K. Moffat, I. Schoegl , R. L. Speth and B. Weber, "Cantera: An object-oriented software toolkit for chemical kinetics, thermodynamics, and transport processes," Version 2.6.0, 2022. [Online]. Available: https://www.cantera.org.

[27] J. Clarke, M. McGilvray and L. Di Mare, "Numerical model for non-equilibrium shock tube flow," in *Radiation and High Temperature Gases Workshop,* 2022.

[28] J. Clarke, M. McGilvray and L. Di Mare, "Numerical simulation of a shock tube in thermochemical non-equilibrium," *AIAA SCITECH 2023 Forum,* no. AIAA 2023-1797, 2023.

[29] B. A. Cruden, A. M. Brandis and M. E. MacDonald, "Characterization of CO Thermochemistry in Incident Shockwaves," *AIAA AVIATION Forum, 2018 Joint Thermophysics and Heat Transfer Conference,* no. 2018-3768, 2018.

[30] C. O. Johnston, "Shock-Layer Radiation Insights Available Through Flowfield-Property Binning," *AIAA SCITECH 2022 Forum,* no. 2022-2396, 2022.

[31] S. Gordon and B. McBride, "Computer program for calculation of complex chemical equilibrium compositions and applications. Part 1: Analysis," NASA RP-1311, 1994.

[32] E. Whiting, C. Park, L. Yen, J. Arnold and J. Paterson, "NEQAIR96,Nonequilibrium and Equilibrium Radiative Transport and Spectra Program: User's Manual," Technical Report NASA RP-1389, Ames Research Center, Moffett Field, 1996.

[33] B. J. McBride and S. Gordon, "Computer Program for Calculation of Complex Chemical Equilibrium Compositions and Applications II. User's Manual and Program Description," *NASA RP-1311-P2,* June 1996.